40307

National Library of Canada / Bibliothèque nationale du Canada

CANADIAN THESES ON MICROFICHE / THÈSES CANADIENNES SUR MICROFICHE

NAME OF AUTHOR/*NOM DE L'AUTEUR* SAEID SHAMMASS

TITLE OF THESIS/*TITRE DE LA THÈSE* AN INVESTIGATION OF UV PREIONIZED DISCHARGE PUMPED LASERS

UNIVERSITY/*UNIVERSITÉ* University of Alberta

DEGREE FOR WHICH THESIS WAS PRESENTED/ *GRADE POUR LEQUEL CETTE THÈSE FUT PRÉSENTÉE* M.Sc.

YEAR THIS DEGREE CONFERRED/*ANNÉE D'OBTENTION DE CE GRADE* 1978

NAME OF SUPERVISOR/*NOM DU DIRECTEUR DE THÈSE* Dr. H. J. J. SEGUIN

Permission is hereby granted to the NATIONAL LIBRARY OF CANADA to microfilm this thesis and to lend or sell copies of the film.

The author reserves other publication rights, and neither the thesis nor extensive extracts from it may be printed or otherwise reproduced without the author's written permission.

L'autorisation est, par la présente, accordée à la BIBLIOTHÈQUE NATIONALE DU CANADA de microfilmer cette thèse et de prêter ou de vendre des exemplaires du film.

L'auteur se réserve les autres droits de publication; ni la thèse ni de longs extraits de celle-ci ne doivent être imprimés ou autrement reproduits sans l'autorisation écrite de l'auteur.

DATED/*DATÉ* Oct. 16th 1978 SIGNED/*SIGNÉ* Saeid Shammas

PERMANENT ADDRESS/*RÉSIDENCE FIXE* Box 621 Sub 11
U of A
Edmonton, Alta, Canada
T6G 2E0

NL-91 (3-74)

National Library of Canada

Cataloguing Branch
Canadian Theses Division

Ottawa, Canada
K1A 0N4

Bibliothèque nationale du Canada

Direction du catalogage
Division des thèses canadiennes

NOTICE

The quality of this microfiche is heavily dependent upon the quality of the original thesis submitted for microfilming. Every effort has been made to ensure the highest quality of reproduction possible.

If pages are missing, contact the university which granted the degree.

Some pages may have indistinct print especially if the original pages were typed with a poor typewriter ribbon or if the university sent us a poor photocopy.

Previously copyrighted materials (journal articles, published tests, etc.) are not filmed.

Reproduction in full or in part of this film is governed by the Canadian Copyright Act, R.S.C. 1970, c. C-30. Please read the authorization forms which accompany this thesis.

THIS DISSERTATION
HAS BEEN MICROFILMED
EXACTLY AS RECEIVED

AVIS

La qualité de cette microfiche dépend grandement de la qualité de la thèse soumise au microfilmage. Nous avons tout fait pour assurer une qualité supérieure de reproduction.

S'il manque des pages, veuillez communiquer avec l'université qui a conféré le grade.

La qualité d'impression de certaines pages peut laisser à désirer, surtout si les pages originales ont été dactylographiées à l'aide d'un ruban usé ou si l'université nous a fait parvenir une photocopie de mauvaise qualité.

Les documents qui font déjà l'objet d'un droit d'auteur (articles de revue, examens publiés, etc.) ne sont pas microfilmés.

La reproduction, même partielle, de ce microfilm est soumise à la Loi canadienne sur le droit d'auteur, SRC 1970, c. C-30. Veuillez prendre connaissance des formules d'autorisation qui accompagnent cette thèse.

LA THÈSE A ÉTÉ
MICROFILMÉE TELLE QUE
NOUS L'AVONS REÇUE

NL-339 (3/77)

THE UNIVERSITY OF ALBERTA

AN INVESTIGATION OF UV PREIONIZED DISCHARGE PUMPED LASERS

by

(C) SAEID SHAMMASS

A THESIS

SUBMITTED TO THE FACULTY OF GRADUATE STUDIES IN PARTIAL

FULFILMENT OF THE REQUIREMENTS FOR THE DEGREE

OF MASTER OF SCIENCE

DEPARTMENT OF ELECTRICAL ENGINEERING

EDMONTON, ALBERTA

FALL, 1978

THE UNIVERSITY OF ALBERTA

FACULTY OF GRADUATE STUDIES AND RESEARCH

The undersigned certify that they have read, and recommend to the Faculty of Graduate Studies and Research, for acceptance, a thesis entitled AN INVESTIGATION OF UV-PREIONIZED DISCHARGE PUMPED LASERS submitted by SAEID SHAMMASS in partial fulfilment of the requirements for the degree of Master of Science in Electrical Engineering.

.....
Supervisor

.....

.....

.....

.....

Date September 11.....1978

ABSTRACT

A corrosive resistant system is designed for studying the uv-preionized lasers, including rare-gas halide lasers.

To permit the utilization of ordinary gauges irrespective of the corrosiveness of the gases in the chamber, an isolating device is designed as an interface between the chamber and the gauges.

A novel simple microwave diagnostic technique is established, its validity is demonstrated, and it is applied to photo-electron density measurements.

Finally, a numerical method is found for analyzing the data obtained from photo-electron density measurements. The effect of photoionization, diffusion, attachment, and recombination occurring simultaneously, and the relative importance of each in the laser applications are investigated; the initial diffusion of the electrons plays an important role in some laser applications.

ACKNOWLEDGEMENTS

The author wishes to faithfully thank Professor H.J.J. Seguin for his constant cooperation, guidance, and encouraging advice throughout the work. The author is also grateful to Dr. V. Merchant for his assistance and patience in many fruitful discussions about the work, and thankful to Mr. J. Radzion for his assistance in setting up the electronics needed for the capacitance null detector. The author also thanks Mr. K. Doerrbecker and his staff for their excellent help in the machine shop, and thanks his wife Sherrie for typing this thesis.

TABLE OF CONTENTS

CHAPTER		PAGE
I.	INTRODUCTION	1
	Rare-gas Halide Lasers	5
II.	EXPERIMENTAL SETUP	11
	Vacuum System	11
	Null Detector	14
	UV Source	21
	Plasma Diagnostic Device	27
III.	THE MICROWAVE ATTENUATION DIAGNOSTIC TECHNIQUE	36
	Conclusions	38
IV.	THE ANALYSIS OF THE DATA	42
	Experimental Verification	60
	Conclusions	

***

REFERENCES 62

LIST OF TABLES

Table	Description	Page
4-1	The results of computer calculations for the data of Fig 4-1	49

LIST OF FIGURES

Figure		Page
1-1	Potential energy curves for XeF	7
1-2	Calculated potential energy curves for KrF	10
2-1	The experimental setup	12
2-2	The vacuum system	13
2-3	Cross-sectional view of the capacitance manometer	16
2-4	Diaphragm null capacitance vs. operating pressure	17
2-5	Diaphragm capacitance vs. pressure differential	18
2-6	The capacitance null detector	20
2-7	The uv source	22
2-8	The microwave interferometer	24
2-9	The microwave attenuation diagnostic device	26
3-1	Microwave attenuation vs. frequency	30
3-2	UV photoionization at 11.9 Torr of air; the attenuation vs. time is measured at various frequencies	32
3-3	Photo-electron density vs. time in He	33
3-4	Photo-electron density vs. time in N_2	34
3-5	Photo-electron density vs. time in air	35
4-1	Photo-electron density vs. time in CO	46
4-2	Variation of (B/A) P with pressure for the data of Fig 4-1	50
4-3	ln(A) vs. pressure for the data of Fig 4-1	51
4-4	Photo-electron density vs. time in Tri-n-propyl Amine	54

4-5	(B/A) P vs. pressure for the data of Fig 4-4	55
4-6	ln(A) vs. pressure for the data of Fig 4-4	56
4-7	Photo-electron density vs. time in N_2	57
4-8	(B/A) P vs. pressure for the data of Fig 4-7	58
4-9	ln(A) vs. pressure for the data of Fig 4-7	59

LIST OF SYMBOLS

Physical Constants:

ε_o: dielectric constant of free space

c: speed of light in free space

e: electronic charge

m: electronic mass

Symbols:

α recombination coefficient

β attachment coefficient

γ constant indicating photo-electron generation per pressure, due to the uv source

η penetration depth of a uv light in a gas per pressure

μ refractive index of a plasma

σ decay rate of the current in a uv source

ω the radian frequency of the current in a uv source

ω_o the radian frequency of an electromagnetic wave traversing a plasma

$^2\Sigma_{1/2,3/2,\ldots}$: electronic states of a molecule considering the symmetries of the molecule; the upper left index shows the total spin, and the lower right index shows the total angular momentum

$A_{1/2}, B_{3/2},\ldots$: electronic states of a molecule, spin orbit interaction also considered

$A(f_o)$ attenuation of an electromagnetic wave (with frequency f_o) because of the multiple reflections at the

chamber walls

C_o: capacitance of a manometer when the pressures at both sides are equal

C: capacitance of a manometer when the pressures at the two sides are unequal

D_e: electron diffusion coefficient

D_p: ion diffusion coefficient

E: electric field of a wave traversing a plasma

f_o: frequency of a wave traversing a plasma

I: current in a uv source

I_o: amplitude of the current in a uv source

J: current density because of the motion of electrons in a plasma

k: propagation constant of an electromagnetic wave in a plasma

k_o: propagation constant of an electromagnetic wave in free space

N: initial electron density profile in a plasma generated by a uv source

n_e: electron density

$\bar{n}_e$: average electron density in the direction in which an electromagnetic wave travels in a plasma

n_p: ion density

P: pressure

P_o: operating pressure; the mean pressure of the pressures at the two sides of a capacitance manometer

P_r: pressure at the reference side of a manometer

P_x: pressure at the unknown side of a manometer

ΔP: pressure differential ($=P_r-P_x$)

r: radial distance in a cylindrical chamber

t: time; t=0 is the time at which a uv source is ignited

V_o: output voltage of a capacitance bridge having a manometer at one arm

z: axial direction in a cylindrical chamber

z_m: the distance between a uv source irradiating the gas in a chamber and the axis of the transmitting and receiving antennas for microwave diagnostic purposes

Abbreviations:

e-beam: electron beam

l.f.: low frequency

r.f.: radio frequency

uv: ultra violet

x-tal: crystal

CHAPTER ONE

Introduction

The parameters associated with CO_2 lasers pumped by uv-preionized discharges are thoroughly investigated by McKen, Seguin, and Tulip [1]. McKen [2] has given an interesting and thorough history of the development of uv-preionized lasers.

In the first CO_2 laser [2] the excitation was longitudinal to the laser axis and required an electric field to pressure ratio of above breakdown for effective pumping. CO_2 laser pulses of 5 J to 200 KW were obtained from a device eight feet long by three inches in diameter.

'Beaulieu, using a row of closely spaced resistors for a cathode and a flat or cylindrical anode, was able to transversely excite an atmospheric pressure mixture of CO_2, N_2, and He. The acronym TEA was used to describe this kind of laser. He was able to obtain pulses of 150 mJ at peak powers of 0.5 MW from a device employing 150 cathode resistors (1000 ohms each). The device was 1.25 m long and the cathode anode spacing was 2.5 cm. It was repeatedly excited by a discharge from a 0.02 μF capacitor charged to 25 KV. The gas mixture was in the ratio $CO_2:N_2:He = 1.2:1:10$. This was a significant step in the development of high power lasers... .

'In order to obtain a more uniform excited density distribution, Beaulieu attempted to initiate a distributed discharge between two long parallel electrodes. An increase in the gas pressure above 20 Torr forced the discharge into an arc.

'A distributed discharge can be obtained with extended electrodes even at atmospheric pressure provided that the discharge time is shorter than the arc formation time...' However, at the experimental conditions of interest the discharge time becomes too long and arcs have time to form. 'In addition a fast discharge time does not correspond to the most efficient pumping rate of CO_2 lasers...'

'An alternative solution to the problem is to prevent the current density from reaching a large enough value to initiate an arc.

'One such device employing this technique is the so called "double discharge device" or D^3. This system makes use of a mesh or grid cathode with a third electrode placed close to it on the side opposite to the anode. A fast low energy discharge is triggered between the cathode and the third electrode producing a cloud of electrons around the cathode. These electrons facilitate the main discharge to the anode by effectively increasing the discharge area and thereby reducing the current density enough to prevent the formation of a constricted arc. Laflamme obtained 9 J per pulse with a peak of 12 MW from a 3.8 m long laser. The output energy density was 5.5 J/l... .

'... a discharge could be stablized if the volume electron-ion production mechanism in the plasma was made independent of the applied electric field through the use of an external ionization source such as high energy e-beam injection or photoionization... .

Following this argument the electrodes were shaped to Rogowski or Bruce profiles and preionization was established by an additional discharge to a trigger electrode in the form of one or more wires parallel to, but laterally displaced from the discharge axis. This resulted in input energies greater than 400 J/l [2]. "... Pearson and Lamberton used this technique and subsequently showed that it was superior to the previously employed D^3 technique. They suggested that the discharge from the wire to the anode provided uv light..." that resulted in uv photoionization. UV-preionized discharge lasers with more powerful uv sources were established [2].

The advantage of uv preionization over e-beam controlled discharge pumping is that "the uv source can operate within the laser gas environment, so there is no need for high vacuum construction. UV control does not require a thin delicate foil window and so scaling to pressures of many atmospheres should be much easier. High voltage sources needed to accelerate electrons in electron guns are not required for uv control. UV sources can be readily constructed in large arrays giving rise to uniform illumination over a large aperture while it is relatively difficult and expensive to construct large area electron guns."

McKen [2] has argued that a one-step ionization of the gases used in a CO_2 laser, due to uv radiation is unlikely and a two- or multiple-step ionization must be the mechanism.

"However, it is quite feasible that an impurity in the laser with a low ionization potential is the agent responsible for volume

photoionization... ."

Babcock et al. [3] have also concluded that only the impurities are ionized due to uv radiation in CO_2 lasers. Therefore, in order to increase the ionization level, it is advisable to seed the laser gas with a small amount of some type of low ionization potential substance which is transparent at the laser wavelength, and has a small cross section for collisional depopulation of the upper laser level [2]. Following this argument, McKen et al. [1] have given a detailed collection of data providing the photoionization of many laser mixes seeded with appropriate seedants.

Burnham et al. [4] applied the uv-preionized discharge technique to rare-gas halide lasers (an introduction to rare-gas halide lasers is given below). Rothe and Gibson [5] did a parametric study of this type of lasers; they also studied the effects of easily ionizable seedants:"... triethylamine and xylene showed no increase in efficiency that could be attributed to these seed gases. However, traces of xylene permitted the discharge delay to be increased from 2 μs to 25 μs with no drop-off in pulse energy. Evidently, the presence of xylene caused a significantly higher level of preionization, so that it took longer for the ion concentration to fall below acceptable levels by ion recombination."

Hsia [6] proposed a model to explain the delay of the main discharge with respect to the uv preionizer in rare-gas halide lasers for optimum operation; "in the model the F^- ions formed by dissociative attachment following uv photoionization, act as a

reservoir from which electrons are easily released, when the main discharge field is applied."

It is the objective of the present work to re-examine the models proposed for uv photoionization and investigate some of its other aspects, seemingly less emphasized in previous works. These aspects include the effect of diffusion, attachment, and recombination acting simultaneously; the work also examines the possibility of interpreting the data obtained by various diagnostic techniques to determine the relative importance of each.

Morever, with the development of rare-gas halide lasers the experimental setup need be corrosive resistant in order to handle corrosive gases such as flourine; the design considerations of such a system are investigated.

Rare-gas halide lasers

The possibility of making lasers by rare gases and halides was first investigated by Velazco and Setser [7]. Soon after, many such lasers - also called excimer lasers - were made. Much research is being carried out in developing these ultraviolet lasers on account of their high power, high efficiency, and the possibility of tuning them in many wavelength ranges. Moreover, their emission is in the blue and ultraviolet, which is of importance for many applications such as isotope separation and photochemistry.

Different pumping techniques such as e-beam, e-beam controlled discharges, and uv-preionized discharges, have been used.

Burnham and Djeu [4] used the uv-preionized discharge technique to excite XeF, krF, and ArF lasers. They obtained laser pulse

energies exceeding 100 mJ with peak powers of several megawatts. 'The discharge in this device had an active length of 60 cm with a cross-sectional area of 2 x 0.5 cm. The chamber was made of lucite, had a volume of about 5 liters, and was equipped with fused silica Brewster's angle windows... . Preionization of the laser medium was obtained from a spark-board photoionization source located at the side of the laser chamber at a distance of approximately 4 cm from the laser axis. Separate triggering of the preionization source and the main discharge allowed the discharge to be fired after the preionization source with a time delay...

'Stimulated emission in XeF was observed on several lines in the principal emission bands at 3511 Å as well as on the three lines of the triplet feature at 3488 Å. Maximum pulse energies of 65 mJ were obtained from gas mixtures containing 0.3% NF_3 and 1% Xe at 1500 Torr.

'Laser pulses with maximum energies of 130 mJ were obtained in KrF. The laser emission had a bandwidth of approximately 3 Å ... . A gas mixture containing 0.3% F_2 and 15% Kr in He at 1500 Torr' was used.'

Brau and Ewing [12] have shown some of the features of XeF lasers in terms of approximate potential-energy curves (Fig 1-1).

'The lowest state is covalent in nature and is slightly bound while the $2^2\Pi_{1/2,3/2}$ states are repulsive.

'Transitions from higher-lying excited states can be either bound to bound, as in the $2^2\Sigma_{1/2} \rightarrow 1^2\Sigma_{1/2}$ 3540 Å or bound to free, as in $2^2\Sigma_{1/2} \rightarrow 1^2\Pi_{1/2,3/2}$.

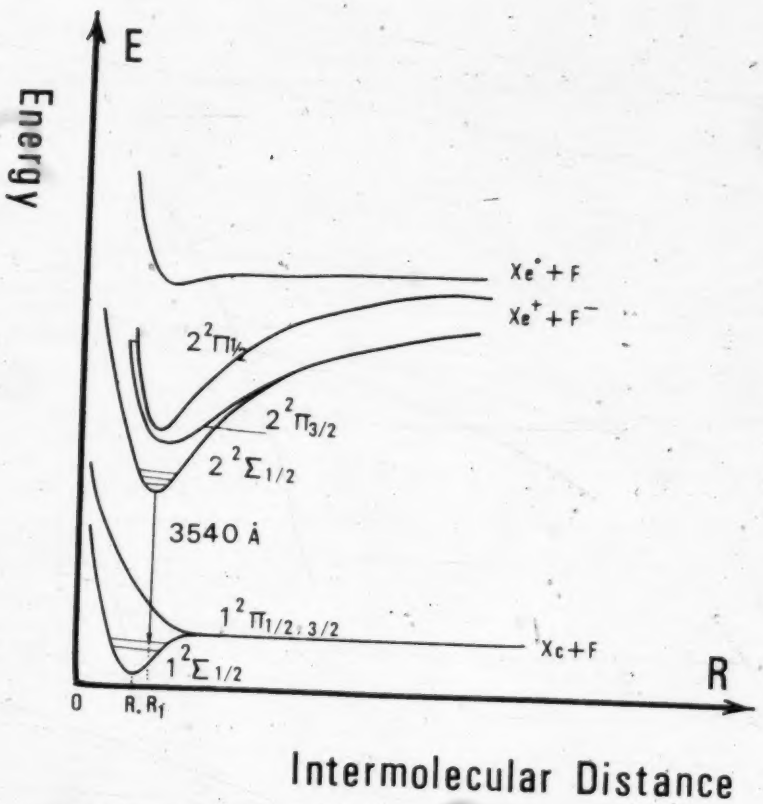

Fig 1-1 Potential energy curves for XeF

'The three higher-lying excited states are predominantly ionic. This ion pair is analogous to an alkali-halide.

'The possibility of laser action on these species is apparently enhanced by a large reaction cross section for producing excited species by chemical reactions of the type

$$Xe^{**} + F_2 \rightarrow XeF^{*} + F$$

'This chemical reaction which starts on an excited potential-energy surface has a high probability of staying on an excited potential surface, producing the electronically excited species with a large rate constant.'

Moreover, Brau and Ewing [8] studied the spontaneous emission spectrum of XeF as a function of pressure and have found that, at pressures above one-half atm the $2^2\Sigma_{1/2}$ states remain in vibrational equilibrium.

'The laser transition $2^2\Sigma_{1/2} \rightarrow 1^2\Sigma_{1/2}$ originates from the lowest vibrational level of the excited state. Since the equilibrium bond length of the excited state (R_1 in Fig 1-1) is larger than that of the ground state, R_o, it is believed that laser transition terminates on a high vibrational level of the lower state. The $2^2\Sigma_{1/2} \rightarrow 1^2\Pi_{1/2,3/2}$ transition is considerably broader since these transitions are bound to free.'

Bhaumik et al. [9] obtained the spectrum of KrF from a mixture of 2 Torr NF_3 and 3.4 atm Ar containing 10% Kr. They reasoned that the absence of any sharp structure in KrF emission spectrum indicates that the transition is of bound to free type.

'The narrow bandwidth (40 Å) of the emission band is understandable in terms of the transition terminating in a relatively flat portion of the repulsive potential curve. Due to a large degree of vibrational relaxation at high pressures emission is expected primarily from the lowest vibrational level of the upper state.'

Brau and Ewing [8] generalized their results to other xenon halides, but Dunning and Hay [10] have argued that, except possibly for XeF, the lower state of rare-gas halides is unbound.

They have calculated the energy levels and distinguish between three possible states (Fig 1-2):

(i) valence limit resulting from the interaction between $Kr(^1s) + F(^2p)$ which is repulsive,

(ii) ionic limit, ionic bond between $Kr^+(^2p) + F^-(^1s)$, and

(iii) Rydberg limit, resulting from the interaction between $Kr^*(^3p) + F(^2p)$.

Their calculations support the previous semiemperical results, but also indicate that the case of KrF is more complicated.

The effect of spin-orbit interaction is taken into account in these calculations; for this reason, the states are named X, A, B, C, and D. The states D and C are superpositions of $2^2\Sigma$ and $2^2\Pi$ states; neglecting spin-orbit interaction, these two states are nearly degenerate - in contrast to Fig 1-2. $B_{3/2}$ state is, however, composed only of $2^2\Pi$ state.

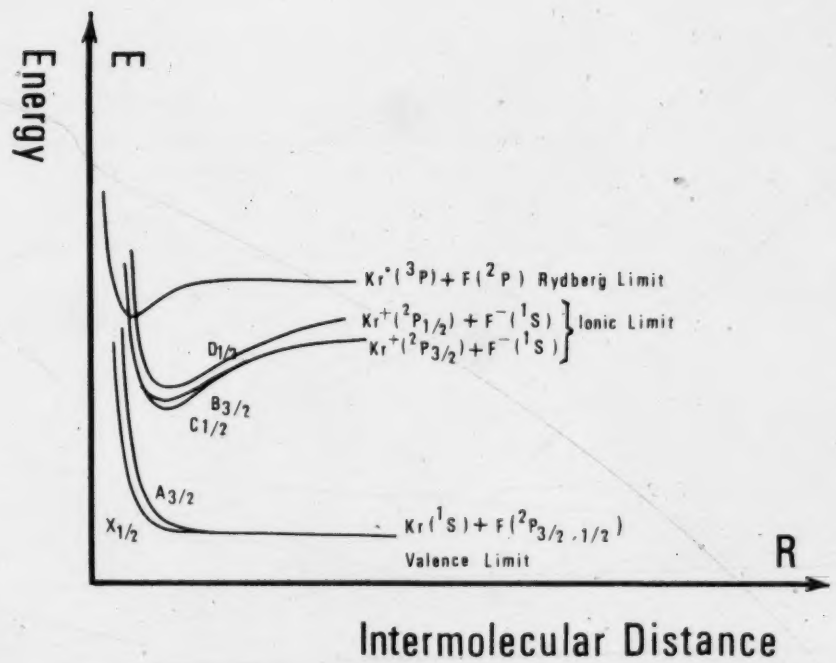

Fig 1-2 Calculated potential energy curves for KrF.

CHAPTER TWO

Experimental Setup

An experimental setup is designed to simulate, and to provide a means to study, the uv preionization. It is desirable to have a setup capable of maintaining gas mixtures of the required pressures. The gas mixture can then be irradiated by a uv source; the gas mixture is ionized and a transient plasma is produced. A suitable plasma diagnostic device is needed to measure the electron density fluctuations in the plasma. An experimental setup consisting of three main sections is designed to meet these requirements (Fig 2-1):

vacuum system: to contain and maintain the desired pressure of the gas mixture needed,

uv source: to produce uv radiation needed for photoionizing the gas mixture,

plasma diagnostic device: to measure fluctuations of electron density generated by the uv source.

These sections are explained in more detail below.

Vacuum system

The vacuum system is shown in Fig 2-2. It is designed for handling corrosive gases, such as flourine [11].

The chamber is made of a lucite pipe with a wall thickness of 0.75 cm, an internal diameter of 14 cm and 12.7 cm long, closed by a lucite disk and an aluminum disk in which proper threaded holes are devised for the gas inlet, outlet, and gauge connections. There is also a window at the center for the spark plug, necessary to photoionize the gas in the chamber. The three pieces are held tightly

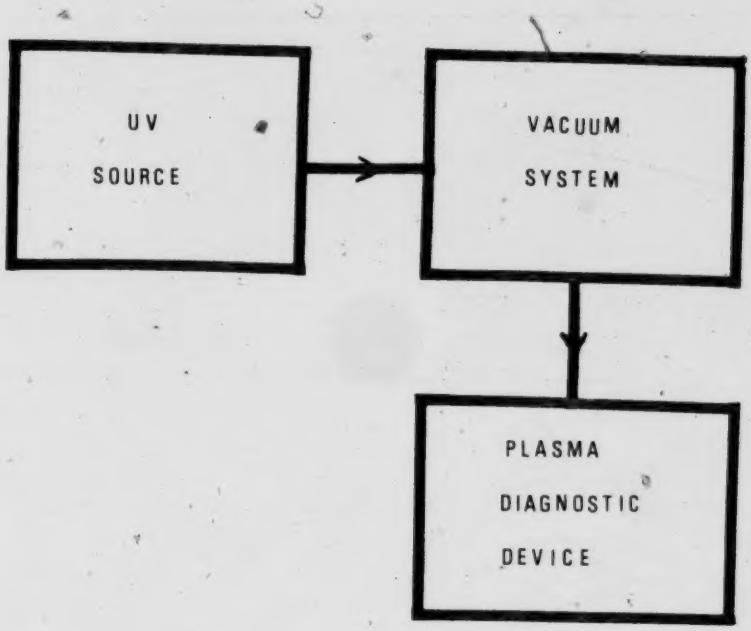

Fig 2-1 The experimental setup.

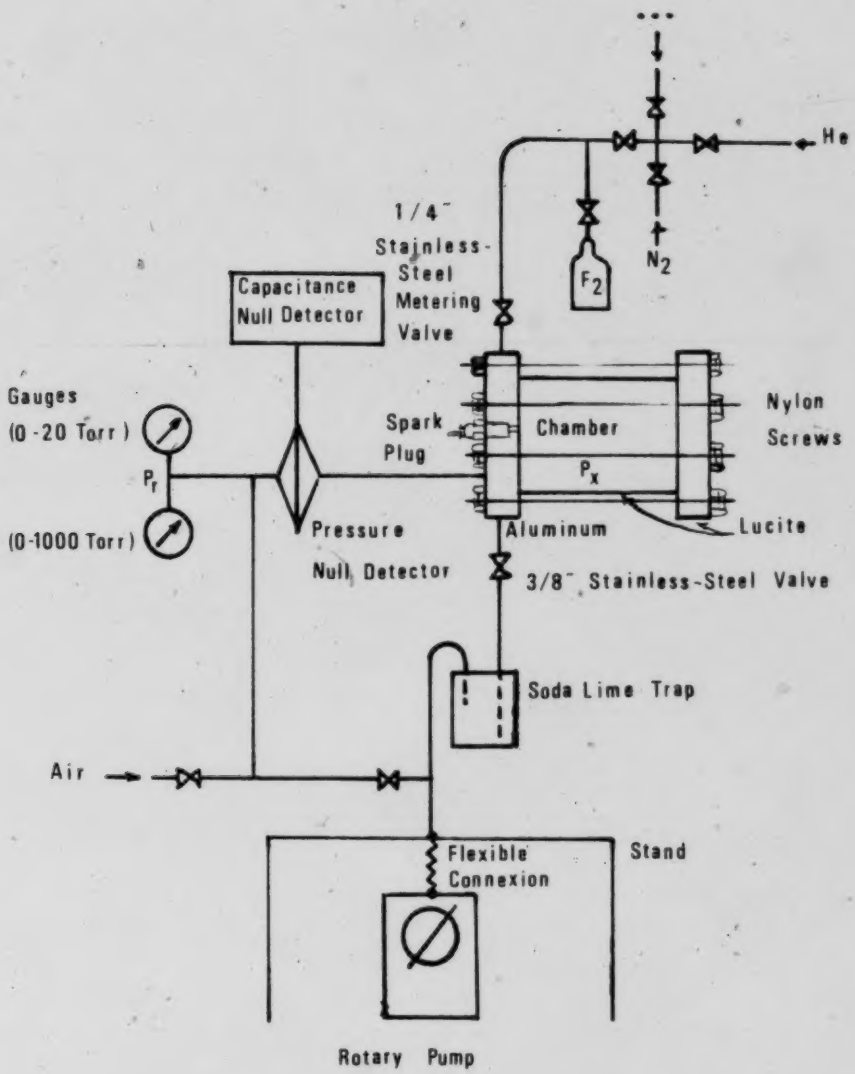

Fig 2-2 The vacuum system.

together by six nylon screws 1.25 cm in diameter. Teflon tape and o-rings are used on account of their corrosive resistance.

The valves which are directly in contact with corrosive gases are stainless steel. The lines and fillings are connected to each other, either by swedgelock or silver soldering [11].

A soda lime trap - a cylinder, 10 cm in diameter, and 10 cm long - is designed to absorb trace amounts of flourine and protect the rotary pump [11].

A flexible connexion, fixed at one end to a heavy stand, is used at the input of the rotary pump to isolate the system from the vibrations of the pump; this is particularly necessary otherwise excessive vibration of the pipes would make them vulnerable to flourine attacks [11].

In order to use the standard noncorrosion resistant gauges already available, a null detector was designed to isolate the chamber from the gauges and at the same time indicate whether the pressure shown by the gauge, P_r, is the same as the pressure in the chamber, P_x. The null detector is discussed in more detail below.

Null detector [12]

The null detector is a specialized differential-pressure capacitance manometer; its capacitance changes with $\Delta P = P_r - P_x$. It consists of two parts; the pressure null detector and the capacitance null detector.

The pressure null detector consists of two aluminum disks 15 cm in diameter, having many pinholes at the center and an aluminum

foil sandwiched between two thin F.E.P. layers (Fig 2-3). F.E.P. is a dupont flourinated ethylene propenol having the chemical resistance of teflon and mechanical properties similar to mylar.

As ΔP changes, the inner layers move from the central position inside the space devised between the disks;the space is designed so that the teflon layers remain within their elastic limits.

The two aluminum disks are bolted together, by eight metalic screws, for vacuum tightness. They are hence also electrically connected, and form one side of the capacitor, the other side being, of course, the aluminum foil.

For symmetry reasons the lowest capacitance, C_o, of the device corresponds to the position in which the layers are centrally located, and therefore to the state $\Delta P=0$, regardless of the operating pressure.

However, as the operating pressure, P_o, decreases the air trapped in between the teflon layers will exhibit a pressure comparable to P_o, and the position of the aluminum foil will be loosely defined. This would result in a hysteresis effect in C_o vs. P_o. To omit this effect, a few small holes were devised in the F.E.P. layer on the gauge side. Fig 2-4 shows C_o plotted vs. P_o.

The device is sensitive to a ΔP in the order of 10^{-3} Torr. It is also possible to calibrate the device for $\Delta P \neq 0$. Fig 2-5 shows the change in the capacitance, C, with ΔP.

The measurements of Figs 2-4 and 5 were carried out by a common universal bridge, and a standard differential pressure manometer.

Fig 2-3 Cross-sectional view of the capcitance manometer

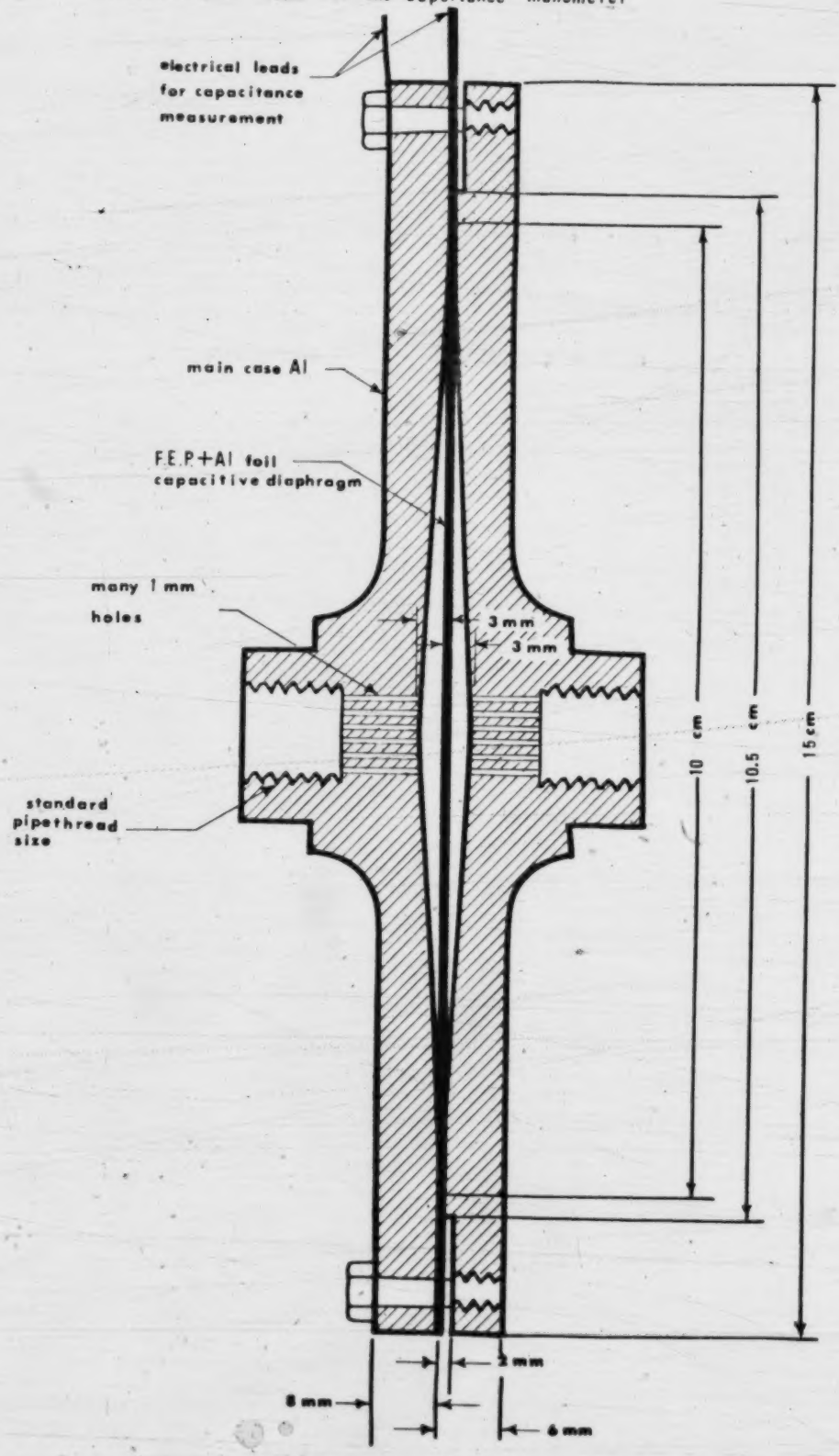

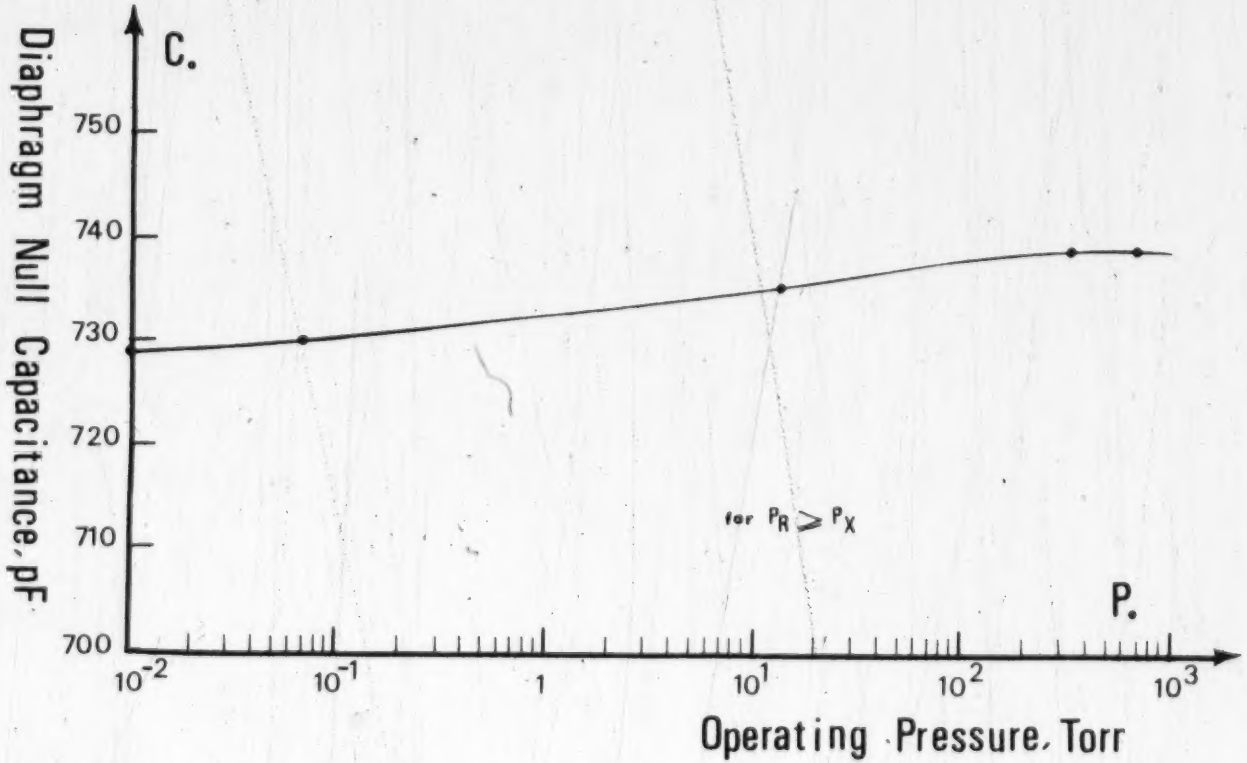

Fig 2-4 Diaphragm null capacitance vs. operating pressure.

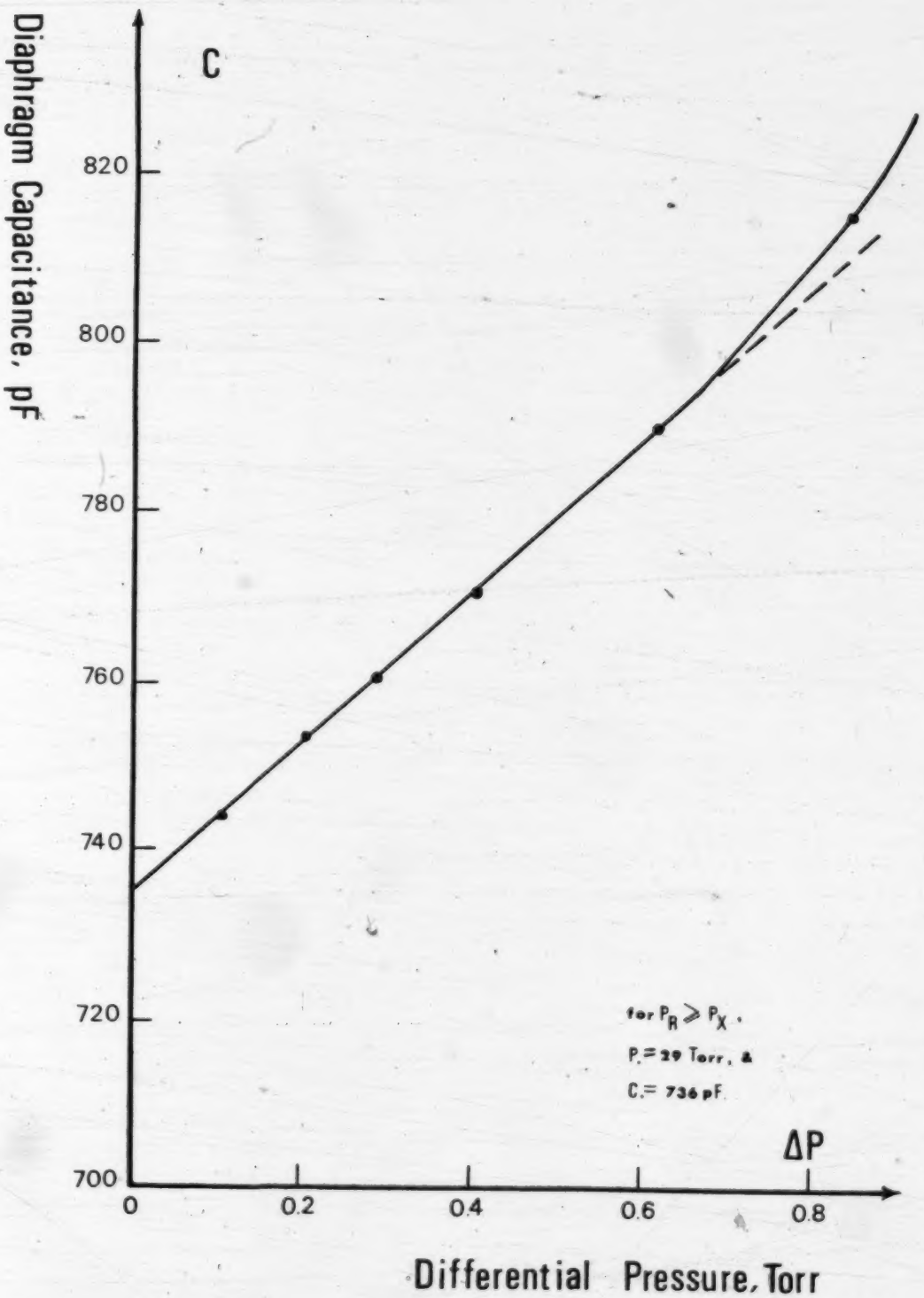

Fig 2-5 Diaphragm capacitance vs. pressure diffential.

The capacitance null detector was designed to indicate when $\Delta P=0$. The block diagram is shown in Fig 2-6.

The pressure null detector is connected to one arm of a capacitance bridge (Fig 2-6). A 5 KHz Wien-bridge oscillator feeds the bridge, and if the bridge is balanced, then the bridge output voltage, V_o, will be zero and the two LED's will be off, otherwise they are on.

As C changes, due to pressure changes, V_o will be nonzero and will be amplified by the logarithmic-gain amplifier. The buffer, having a high input impedance, prevents the bridge from being loaded. The logarithmic-gain amplifier has a much higher gain for low voltage levels, so that when the bridge is close to being balanced the precision will increase.

The narrow-band bandpass filter, tuned for 5 KHz, reduces the noise and amplifies only those signals which have afrequency of 5 KHz.

The logic circuit compares the output of the filter to two certain levels one higher than the other; if the voltage is under the "higher" level, LED1 will turn off; if it is under the "lower" level, LED2 will turn off. Thus, LED1 indicates rough bridge adjustments, corresponding to 10^{-2} Torr, while LED2 indicates very precise bridge adjustments, corresponding to 10^{-3} to 10^{-4} Torr.

In normal use, both sides - the chamber and the gauge - are pumped down. Air is then leaked into the gauge side up to the desired pressure. Finally the corrosive gas is filled into the chamber until the LED indicators turn off.

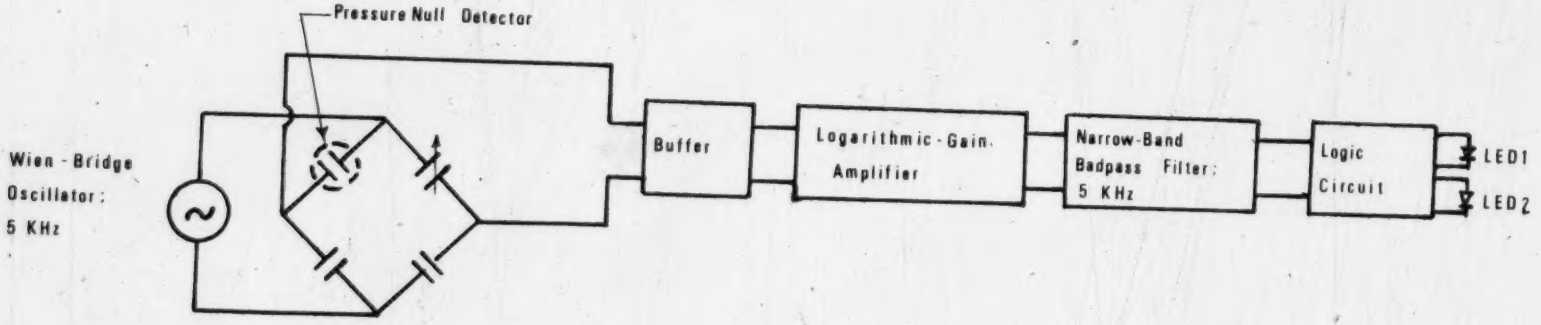

Fig 2-6 The capacitance null detector.

UV source

The uv source in these experiments is fully described by McKen [2]. The design, however, is to some extent modified (Fig 2-7).

The high voltage power supply causes the pressurized spark gap to break down at a voltage dependent on the interelectrode distance and the pressure of N_2, thus causing a short circuit at one terminal of C, and a damped oscillatory current to flow in the spark plug, generating uv radiation. In this design, the ballast resistor is encorporated in the same oil filled lucite box as contains the pressurized spark gap and the capacitors. The capacitance is reduced to 0.05 μF, thus increasing the ringing frequency to 1.43 MHz.

Moreover, in the previous work [2], the pressurized spark gap was triggered by a third terminal; in this design the third electrode and the corresponding circuitry is omitted because it generated a lot of noise, both at low frequencies and at radio frequencies. The breakdown in the pressurized spark gap is repetitive and adjustable by the interelectrode distance and the pressure of N_2. This omission reduced the noise by a factor of 10^3.

Plasma diagnostic device

Two different diagnostic methods were used. The well known microwave interferometer, and a new microwave attenuation method.

The microwave interferometer, as discussed by McKen [2] and Seguin et al. [13], is slightly modified and is shown in Fig 2-8.

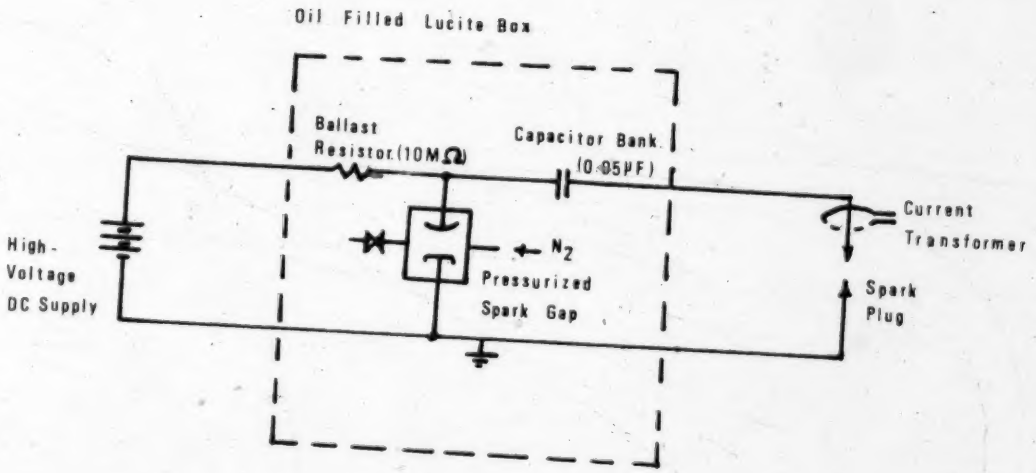

Fig 2-7 The uv source.

The output of the klystron K01 is split into two parts by the 10 dB directional coupler. One part traverses the chamber via the horn antennas (test arm) and undergoes a phase shift and an attenuation depending on the ionization level of the gas in the chamber; the other part is passed through a variable phase shifter and a variable attenuator (reference arm).

The output from the reference arm is subtracted from that of the test arm by the magic T. Initially, the chamber is evacuated and the bridge is balanced (i.e. the output of the magic T is made to be zero) by adjusting the variable phase shifter and the variable attenuators. As the chamber is filled with the desired gas(es) and is irradiated by the uv source, there will be a deviation in the phase and the attenuation in the output of the test arm, and the output of the magic T will be nonzero.

In order to increase the sensitivity of the interferometer, the output of the magic T is first mixed in the r.f. mixer with a frequency which is 200 MHz different from the output of K01 and which is generated by K02. The 200 MHz output of the r.f. mixer is once more detected by the i.f. mixer to produce a 20 MHz signal and is amplified. The output of the i.f. mixer is applied to an oscilloscope. This setup is highly sensitive and can detect phase shifts in the order of 10^{-3} degree.

The klystrons are oil cooled to prevent frequency shifts due to heating. The isolators are inserted to prevent reflections disturbing the klystrons, and also to suppress unwanted multiple

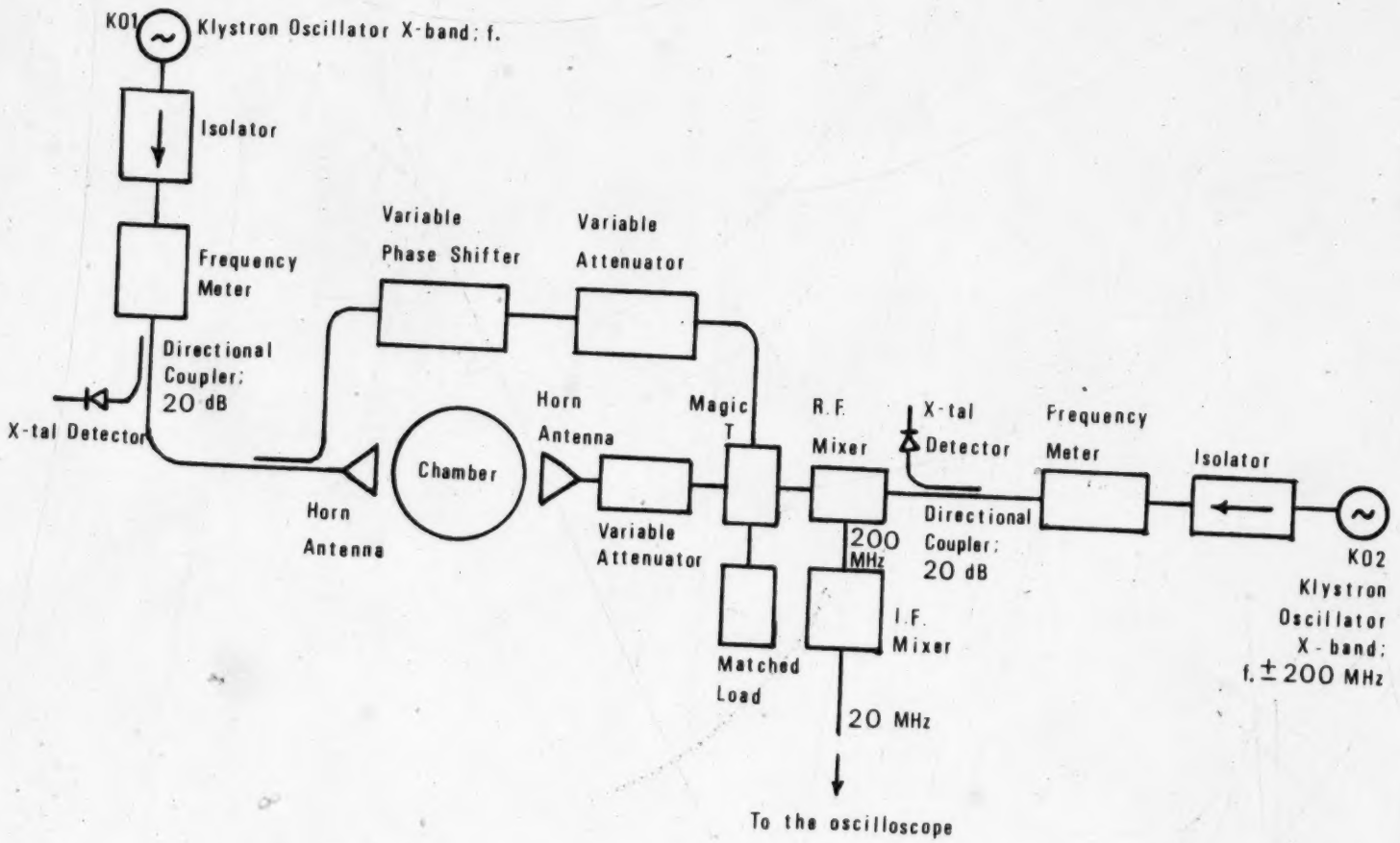

Fig 2-8 The microwave interferometer.

reflections.

The frequency of the klystrons are adjusted by the frequency-meters together with the 20 dB directional couplers and the x-tal detectors.

In the microwave attenuation method (Fig 2-9) the output of the klystron traverses the chamber via the horn antennas and is detected by the x-tal detector. The isolators are inserted to prevent unwanted reflections.

The output of the x-tal detector is applied to the oscilloscope, which is triggerred by the current in the spark plug, via the current transformer of Fig 2-7.

As soon as the spark source irradiates the gas mixture in the chamber, the gas mixture will be ionized; the electrons thus produced, attenuate and change the phase of the microwave radiation. The attenuation is detected by the x-tal detector.

Attenuation of an electromagnetic wave in a plasma may be due to the electron collision frequency [14]. In the next chapter, however, we shall prove that the attenuation measured in certain setups can be due merely to the electron density.

The electron density fluctuations are thus displayed on the oscilloscope and can be photographed.

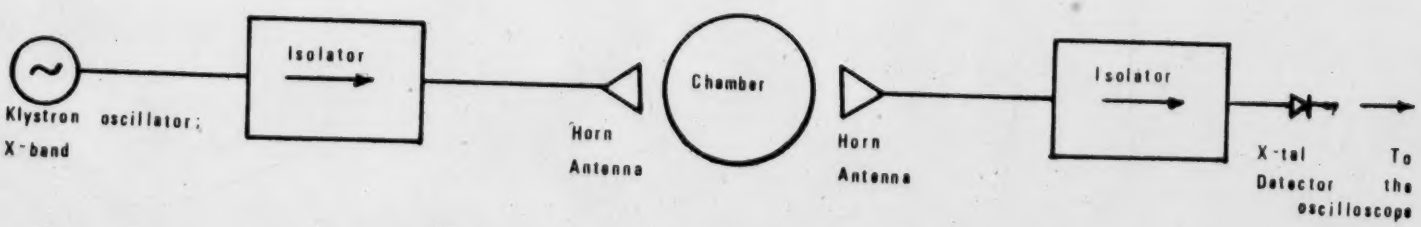

Fig 2-9 The microwe attenuation diagnostic device.

CHAPTER THREE

The Microwave Attenuation Diagnostic Technique

The analysis of the photo-plasmas under experiment is rather easy. It is assumed that [2]

electrons interact with each other only through collective spacecharge forces;

the heavier neutrals and ions are at rest;

collisions of the electrons with the heavy neutrals and ions are negligible;

the plasma is "cold" and relativistic effects can be ignored;

the plasma density fluctuations are slow compared to the frequency of the TEM wave traversing the plasma so that steady-state solutions can be considered.

The experimental results of this chapter dmonstrate the validity of the above assumptions.

The case of an infinite plasma is considered first; the effect of multiple reflections in an unbound plasma is considered then.

The electrons in the plasma are thus only affected by the electric field, E, of the TEM wave traversing the plasma [14]. From Newton's law of motion

$$-e \cdot E = m \cdot \ddot{x} \qquad (3\text{-}1)$$

where

m is the electronic mass,

e is the electronic charge, and

x is the displacement.

According to the above assumptions the operator d/dt can be replaced by $j\omega_o$, where ω_o is the radian frequency of the wave;

$$\omega_o = 2\pi \cdot f_o \quad . \tag{3-2}$$

Eq 3-1 can be written as

$$m \cdot (j \cdot \omega_o)^2 \cdot x = -e \cdot E$$

or

$$x = e \cdot E / (m \cdot \omega_o^2) \tag{3-3}$$

The current density resulting from electron displacements is

$$J = -n_e \cdot e \cdot \dot{x} \tag{3-4}$$

where n_e is the electron density. Replacing d/dt with $j\omega_o$ Eq 3-4 can be written as

$$J = -j \cdot \omega_o \cdot n_e \cdot e \cdot x \tag{3-5}$$

substituting x from Eq 3-3 into Eq 3-5 results in

$$J = -j \cdot \omega_o \cdot n_e \cdot e^2 \cdot E / (m \cdot \omega_o^2) \tag{3-6}$$

Comparing Eq 3-6 with the Ohm's law, it is noticed that the conductivity is imaginary. Considering Maxwell's equations, an imaginary conductivity acts as a dielectric constant, and can be added to the dielectric constant of the free space when divided by $j\omega_o$; thus the overall dielectric constant is

$$\varepsilon = \varepsilon_o - n_e \cdot e^2 / (m \cdot \omega_o^2) \tag{3-7}$$

where ε_o is the dielectric constant of the free space. Consequently the refractive index will be

$$\mu = [1 - n_e \cdot e^2 / (m \cdot \varepsilon_o \cdot \omega_o^2)]^{1/2} \tag{3-8}$$

Inserting the numerical values of m, e, and ε_o in Eq 3-8 results in

$$\mu = (1 - 8.064 \times 10^7 \cdot n_e / f_o^2)^{1/2} \tag{3-9}$$

where n_e is the electron density in cm^{-3}, and f_o is the frequency of the electromagnetic wave in Hz.

If the second term in the brackets is small compared to unity, Eq 3-9 can be approximated to

$$\mu \approx 1 - 4.032 \times 10^7 \cdot n_e / f_o^2 \qquad (3\text{-}10)$$

The propagation constant of the wave

$$k_o = 2\pi \cdot f_o / c \qquad (3\text{-}11)$$

where c is the speed of light in free space, will accordingly change to

$$k = \mu \cdot k_o \qquad (3\text{-}12)$$

Considering Eqs 3-10,11, and 12, it can be assumed that the change in k_o, because of n_e, is <u>similar</u> to a change in f_o by an amount

$$\Delta f = 4.032 \times 10^7 \cdot n_e / f_o \qquad (3\text{-}13)$$

In the experimental setup of Fig 2-9, the wave is reflected many times back and forth by the chamber walls and the overall attenuation, A, will be a function of the propagation constant, or frequency

$$A = A(f_o) \qquad (3\text{-}14)$$

this function can be found by sweep frequency techniques. For the chamber in these experiments, A is measured for f_o ranging from 9.5 GHz to 10.1 GHz and is plotted in Fig 3-1.

If f_o is kept constant and n_e is changed (due to uv-photoionization), Eq 3-13 suggests that the change in n_e is similar to a change in f_o, and consequently (Eq 3-14) to a change in A;

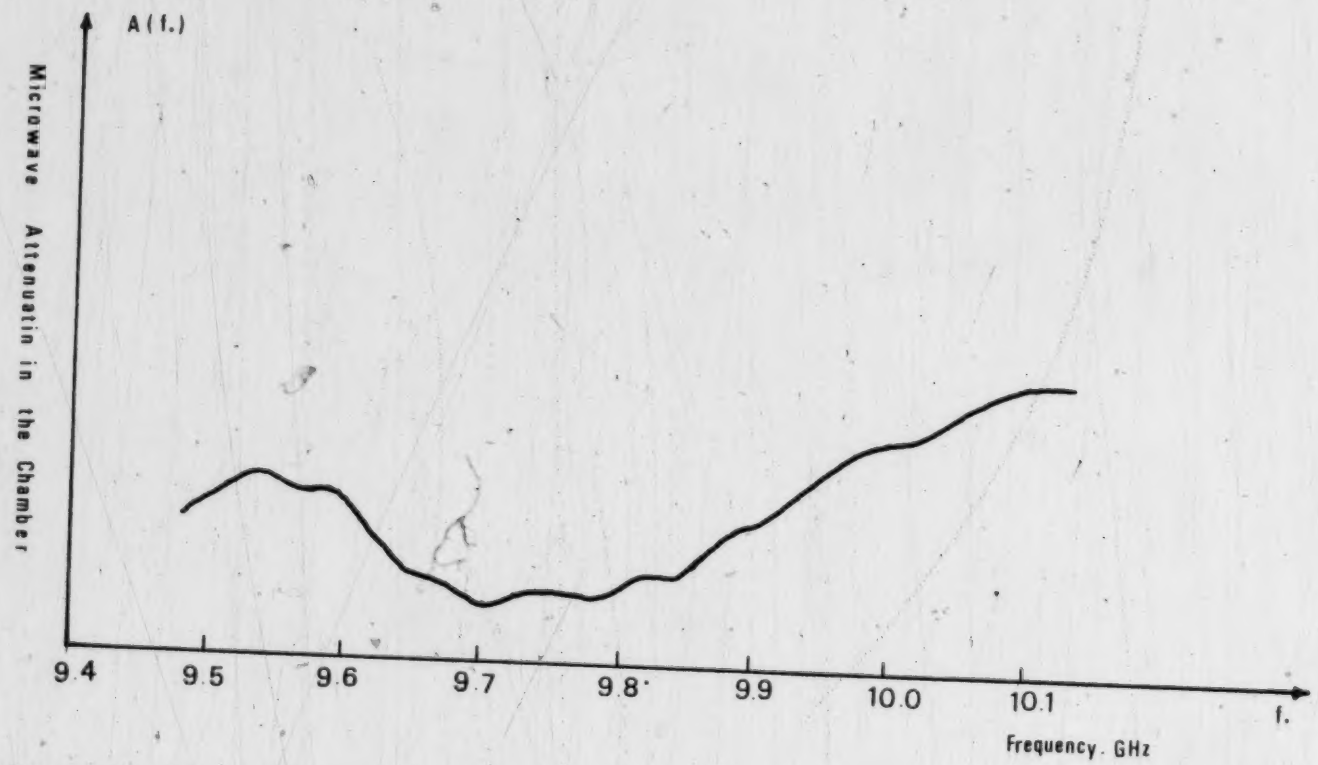

Fig 3-1 Microwave attenuation vs. frequency.

(The attenuation is due to multiple reflections in the chamber)

$$A = A(f_o - \Delta f) \qquad (3\text{-}15)$$

This assumption is valid, if the attenuation is due primarily to the reflections in the chamber alone. To fulfill this condition, the isolators are inserted in Fig 2-9.

Moreover, if the variation of n_e in the radial direction in the chamber is smooth - compared to the wavelength of the electromagnetic wave - the average of n_e in the radial direction, $\bar{n}_e$, can be considered, while using Eqs 3-13 to 15.

To examine the validity of the above assumptions, the chamber (Fig 2-9) was filled with 11.9 Torr of air, and it was irradiated by the uv source. The attenuation was measured at various frequencies keeping all the other conditions unaltered. The experimental results are shown in Fig 3-2 and demonstrate the validity of this procedure.

It can be seen (Figs 3-1, and 2) that the best frequency to perform the experiments at, is 9.95 GHz, because $A(f_o)$ is quite linear at this frequency, and its slope is among the highest.

To calculate the electron density from the detected signals, the slope of $A(f_o)$ should be measured at the operating frequency; for a fixed klystron output, $A(f_o)$ can be measured as the vertical deflection on the oscilloscope; for example, at 9.95 GHz the slope is 36 mV/100 MHz.

Following this procedure the electron densities of He, N_2, and air were found as a result of uv photoionization. The results are shown in Figs 3-3, 4, and 5 respectively.

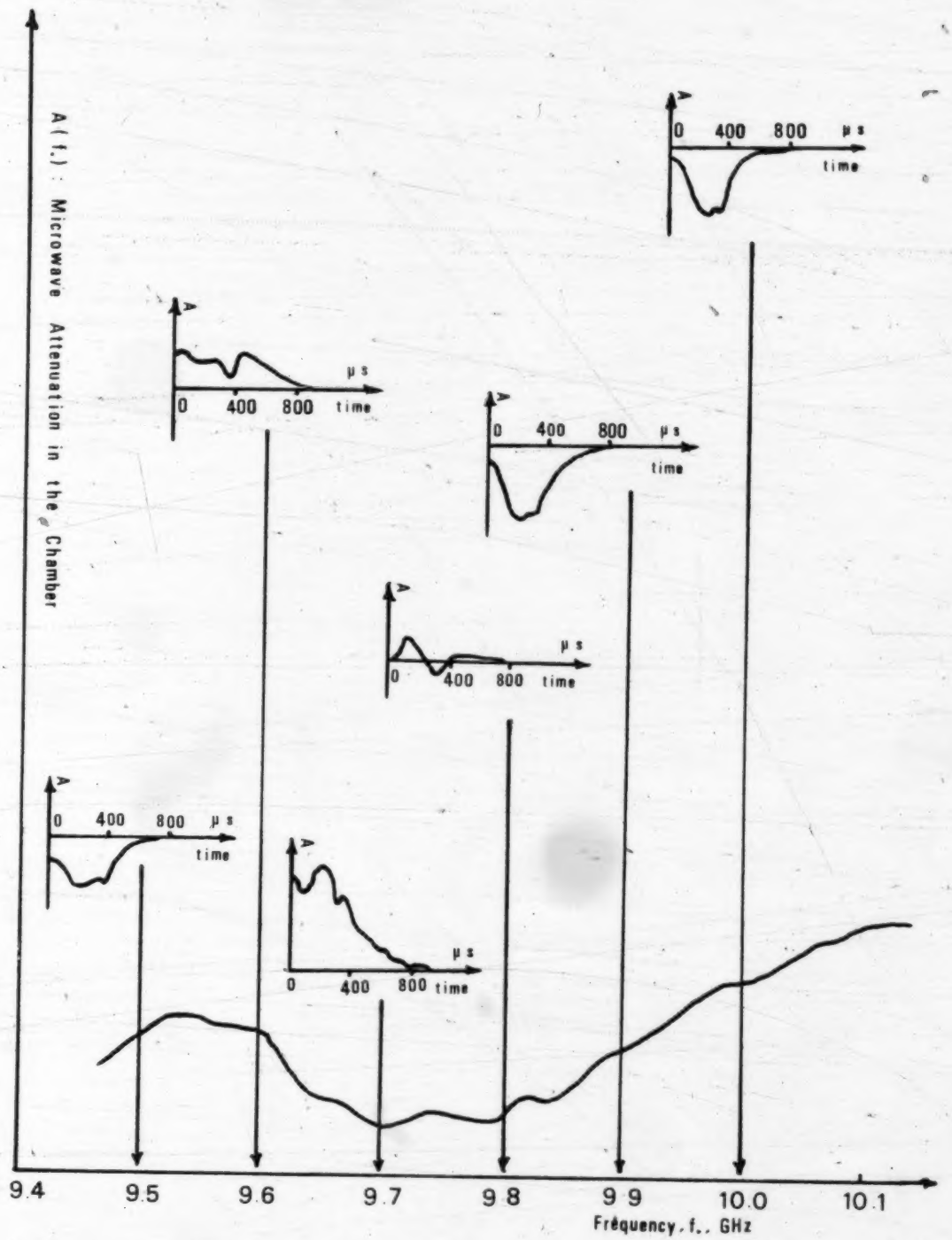

Fig 3-2 UV photoionization at 11.9 Torr of air:

The attenuation vs. time is measured at various frequencies:

The vertical scales are arbitrary.

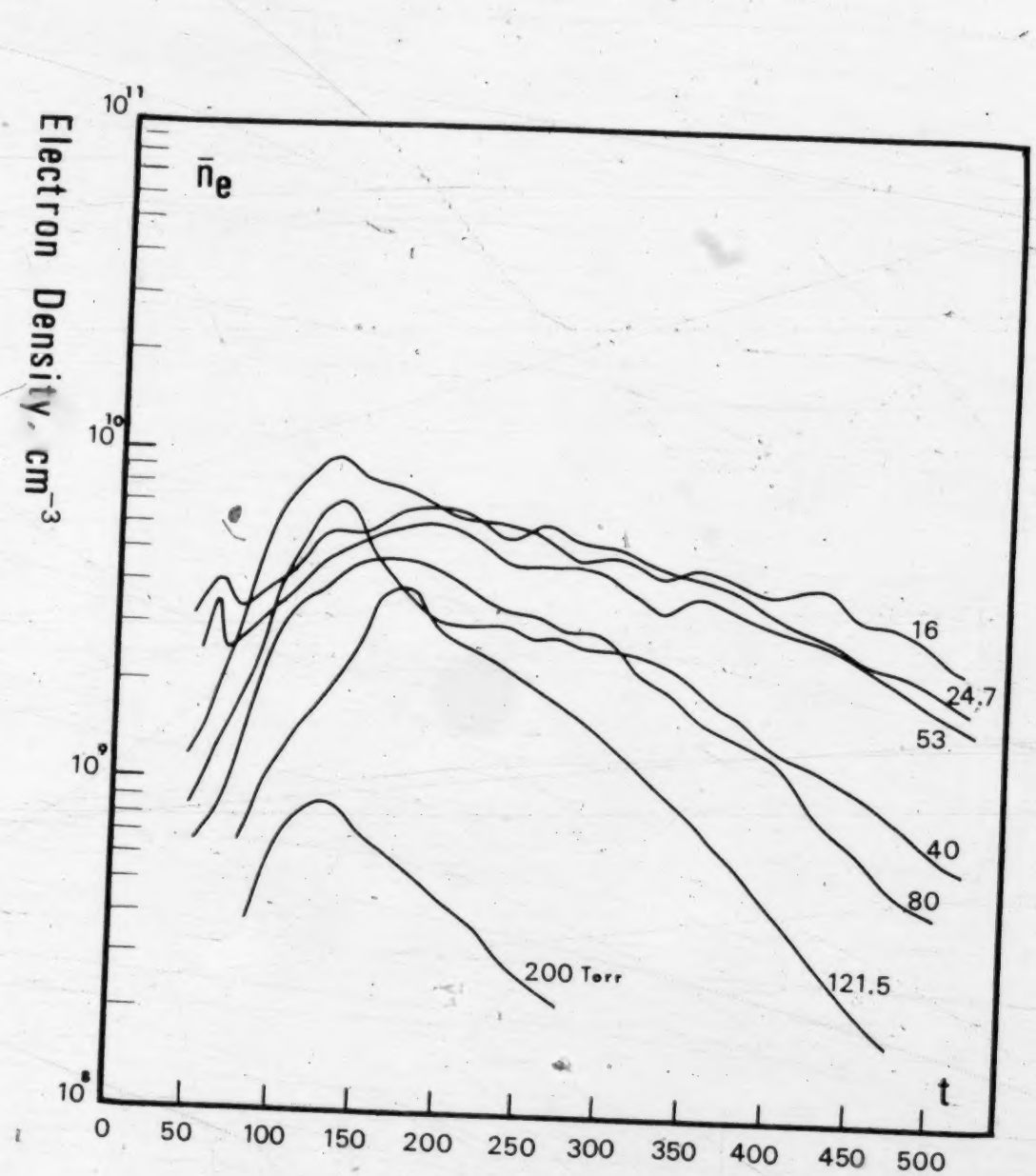

Fig 3-3 Photo-electron density vs. time in He.

axis of horn antennas from uv source (Figs 2-2 & 9): 5 cm.
spark plug voltage: 30 KV

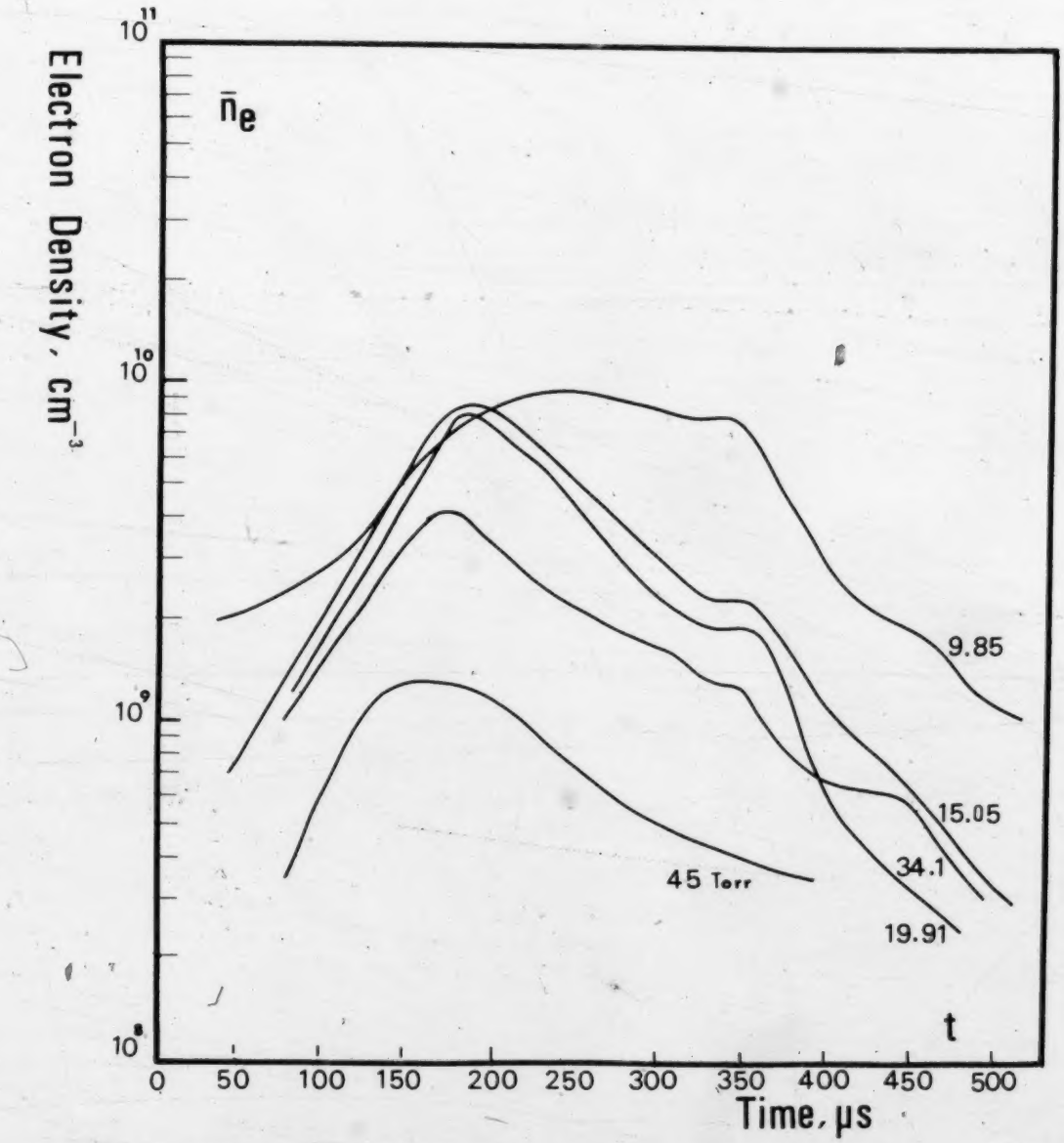

Fig 3-4 Photo-electron density vs. time in N_2.

experimental conditions: same as in Fig3-3

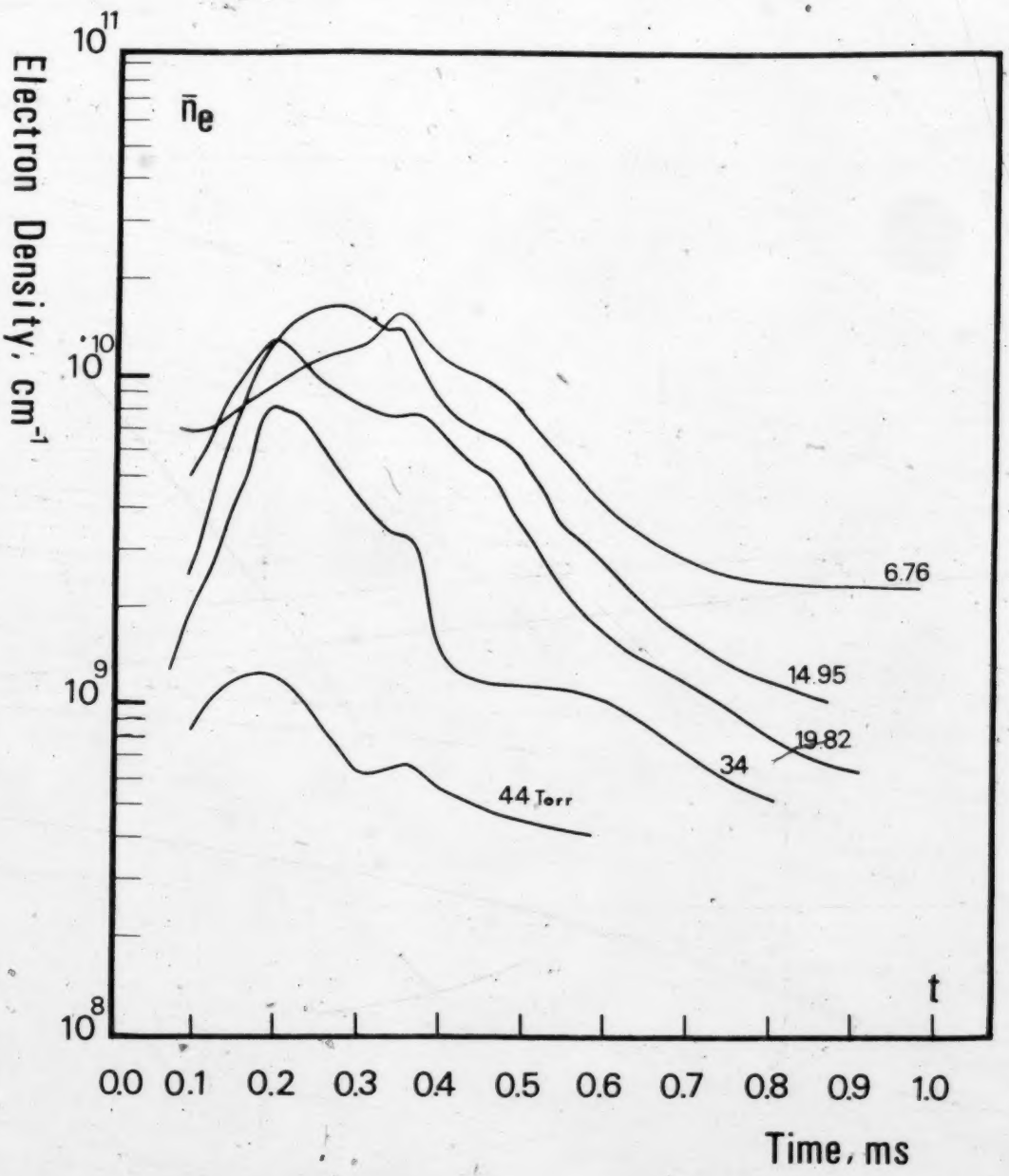

Fig 3-5 Photo-electron density vs. time in air.

experimental conditions: same as Fig 3-3

Conclusions

The microwave attenuation diagnostic technique is a very simple method. The setup needs very few microwave components and can be easily assembled.

There are of course, well known microwave diagnostic techniques, by which the phase and the attenuation of the transmitted wave can be separately measured. However, such setups are extremely elaborate and expensive.

In the conventional microwave interferometer technique, to measure the phase (or attenuation) at each time, the bridge must be balanced by the variable phase shifters and attenuators (Fig 2-8). Thus, to measure the uv-generated electron density in a gas of a certain pressure, the experiment must be performed many times to obtain the electron density as a function of time. In the microwave attenuation technique described in this thesis only one such an experiment is sufficient. This technique, however, is only applicable to those cases in which the electron collisions are negligible.

The main disadvantage of this technique is its sensitivity to noise. In the uv-photoionization experiments the main source of noise is the uv source itself.

The noise generated by the uv source can be classified into two types: the r.f. noise and the l.f. noise. The r.f. noise is generated due to the switching of the pressurized spark gap and that of the spark plug (Fig 2-7). In this setup, this noise decays

exponentially with a time constant of about 20 μs. The l.f. noise seems to be caused by the loading of the mains at the time when the switchings are performed. This noise is coupled via the mains and the ground connections to the klystron and the oscilloscope circuitry.

Due to the l.f. noise the biasings of the electronic circuitry are changed momentarily causing a shift in the klystron frequency and output. In this setup this noise lasts for about 3 μs.

The microwave attenuation technique is very sensitive to both types of noise, so that it was impossible to find the electron densities for times less than 50 μs; t = 0 is the time when the uv source is ignited.

The microwave interferometer, on the other hand, is not very sensitive to the r.f. noise and electron densities can be measured for times as early as 3 μs.

Although shielding the uv source and connecting the grounds by low inductance copper strips to a common point supress the noise to some extent, they are not the ultimate solution to the problem. It may be helpful to connect the measuring electronic circuitry to a regulated supply. It is also advisable to surround the uv source by some microwave absorbing materials, which absorb efficiently in the frequency range of interest.

An interesting extension of the work can be to design a chamber with a predetermined linear transmission in order to obtain the highest sensitivity in a wide frequency range.

CHAPTER FOUR

The Analysis of the Data

The electron density fluctuations, as measured by various diagnostic techniques, are the result of several interacting effects, namely the rate of uv photoionization, electron diffusion, positive ion diffusion, ambipolar diffusion (possibly in the steady state), attachment, and recombination.

Considering all these effects simultaneously, the equations governing the temporal electron and positive ion densities will be

$$\begin{aligned} dn_e/dt &= D_e \cdot \nabla^2 n_e - \alpha \cdot n_e \cdot n_p - \beta \cdot n_e + U \cdot N ; \\ dn_p/dt &= D_p \cdot \nabla^2 n_p - \alpha \cdot n_e \cdot n_p + U \cdot N ; \end{aligned} \qquad (4\text{-}1)$$

where

n_e is the electron density (a function of space and time),

n_p is the positive ion density,

D_e is the diffusion coefficient for the electrons,

D_p is the diffusion coefficient for the positive ions,

α is the recombination coefficient,

β is the attachment coefficient,

U is the rate at which uv light irradiates the gas, and

N is the electron (positive ion) density created by the uv source due to photoionization; N is a function of space.

D_e and D_p are not constants and change with time until they reach the same value, the coefficient of ambipolar diffusion. However, if attention is focused to the initial stage of uv photoionization, which is of prime importance in laser applications, D_e

and D_p can be assumed to be constants.

The current in the spark plug is

$$I = I_o \cdot e^{-\sigma \cdot t} \cdot \sin(\omega \cdot t). \qquad (4\text{-}2)$$

It is logical to assume that U is proportional to I^2;

$$U = 2 \cdot e^{-2 \cdot \sigma \cdot t} \cdot \sin^2(\omega \cdot t). \qquad (4\text{-}3)$$

The coefficient 2 is arbitrarily chosen; U is a rate and any constant associated with it is incorporated in N, for simplicity. Eq 4-3 is in agreement with the fact that the variation in the optical intensity of the uv source ocurres at double the frequency of the current in the spark plug [1].

There is no analytic solution known to Eqs 4-1. A numerical solution, however, can be devised; a power series expansion with respect to time of n_e, n_p, and U can be written about t=0:

$$n_e = \sum_{i=0}^{\infty} n_{ei} \cdot t^i \quad , \qquad (4\text{-}4)$$

$$n_p = \sum_{i=0}^{\infty} n_{pi} \cdot t^i \quad , \qquad (4\text{-}5)$$

where n_{ei} and n_{pi} are the coefficients of expansion (functions of space). The series expansion of Eqs 4-4 and 5 can be performed, if there are no jumps in n_e or n_p with respect to time, in which case they include the transient as well as the steady state solutions. This condition is satisfied since the forcing function U·N in Eqs 4-1 is continuous; U starts from zero (Eq 4-3) at t=0, and changes continuously with time, so n_e and n_p also start from zero and will be continuous. U can be expanded as

$$U = \sum_{i=0}^{\infty} U_i \cdot t^i \qquad (4\text{-}6)$$

U_i can be readily obtained from Eq 4-3:

$$U_o = U_1 = 0 \quad ,$$

$$U_2 = 2 \cdot \omega^2 \quad , \qquad (4\text{-}7)$$

. . . .

Substituting from Eqs 4-4, 5, and 6 into Eq 4-1 the following results are obtained

$$\sum_{i=1}^{\infty} i \cdot n_{ei} \cdot t^{i-1} = D_e \cdot \sum_{i=0}^{\infty} (\nabla^2 n_{ei}) \cdot t^i - \alpha \cdot \sum_{i=0}^{\infty} \sum_{l=0}^{\infty} n_{ei} \cdot n_{pl} \cdot t^{i+l} - \beta \cdot \sum_{i=0}^{\infty} n_{ei} \cdot t^i + N \cdot \sum_{i=0}^{\infty} U_i \cdot t^i \qquad (4\text{-}8)$$

and

$$\sum_{i=1}^{\infty} i \cdot n_{pi} \cdot t^{i-1} = D_p \cdot \sum_{i=0}^{\infty} (\nabla^2 n_{pi}) \cdot t^i - \alpha \cdot \sum_{i=0}^{\infty} \sum_{l=0}^{\infty} n_{ei} \cdot n_{pl} \cdot t^{i+l} + N \cdot \sum_{i=0}^{\infty} U_i \cdot t^i \qquad (4\text{-}9)$$

Equating terms with identical powers of t in Eq 4-8 yields the recursion formula

$$(i+1) \cdot n_{e,i+1} = D_e \cdot \nabla^2 n_{ei} - \alpha \cdot \sum_{k=0}^{i} (n_{ek} \cdot n_{p,i-k}) - \beta \cdot n_{ei} + N \cdot U_i \qquad (4\text{-}10)$$

Similarly, from Eq 4-9

$$(i+1) \cdot n_{p,i+1} = D_p \cdot \nabla^2 n_{ei} - \alpha \cdot \sum_{k=0}^{i} (n_{ek} \cdot n_{p,i-k}) + N \cdot U_i \qquad (4\text{-}11)$$

There is no ionization prior to the ignition of the uv source so n_e and n_p should be zero at t=0; from Eqs 4-4 and 5

$$n_{e0} = 0 \; ; \qquad n_{p0} = 0 \; . \qquad (4\text{-}12)$$

For i=0 Eq 4-10 reduces to

$$n_{e1} = D_e \cdot \nabla^2 n_{e0} - \alpha \cdot n_{e0} \cdot n_{p0} - \beta \cdot n_{e0} + N \cdot U_0 \; . \qquad (4\text{-}13)$$

Inserting the numerical values of n_{e0}, n_{p0}, and U_0 from Eqs 4-7 and 12 into Eq 4-13 it is found that

$$n_{e1} = 0 \; . \qquad (4\text{-}14)$$

Similarly

$$n_{p1} = 0 \qquad (4\text{-}15)$$

For i=1 Eq 4-10 reduces to

$$n_{e2} = D_e \cdot \nabla^2 n_{e1} - \alpha (n_{e0} \cdot n_{p1} + n_{e1} \cdot n_{p0}) - \beta \cdot n_{e1} + N \cdot U_1$$

Considering Eqs 4-7, 12, 14, and 15

$$n_{e2} = 0 \qquad (4\text{-}16)$$

Similarly

$$n_{p2} = 0 \qquad (4\text{-}17)$$

Following this procedure it is found that

$$3 \cdot n_{e3} = 2 \cdot \omega^2 \cdot N \; ; \qquad (4\text{-}18)$$

$$3 \cdot n_{p3} = 2 \cdot \omega^2 \cdot N \; ; \qquad (4\text{-}19)$$

$$4 \cdot n_{e4} = D_e \cdot \nabla^2 n_{e3} - \beta \cdot n_{e3} - 4 \cdot \omega^2 \cdot \sigma \cdot N \; ; \qquad (4\text{-}20)$$

$$4 \cdot n_{p4} = D_e \cdot \nabla^2 n_{p3} - 4 \cdot \omega^2 \cdot \sigma \cdot N \; ; \qquad (4\text{-}21)$$

$$5 \cdot n_{e5} = D_e \cdot \nabla^2 n_{e4} - \beta \cdot n_{e4} + (4 \cdot \omega^2 \cdot \sigma^2 - 2 \cdot \omega^4/3) \cdot N \; ; \qquad (4\text{-}22)$$

. . . .

From Eq 4-18 it is evident that n_{e3} is proportional to the initial electron density distribution due to uv photoionization; n_{e3} averaged inthe radial direction of the chamber can be found as a result of the microwave diagnostic techniques, and a reasonable spatial distribution can be guessed for n_{e3}. Therefore it is necessary to rearrange Eqs 4-18 to 22 in such a form that only partial derivatives of n_{e3} appear in the equations. Thus for example, combining Eqs 4-18 and 20

$$D_e \cdot \nabla^2 n_{e3} - \beta \cdot n_{e3} - 6 \cdot \sigma \cdot n_{e3} - 4 n_{e4} = 0 \; . \qquad (4\text{-}23)$$

From Eq 4-23

$$\nabla^2 n_{e4} = (1/4) \cdot [D_e \cdot \nabla^2 (\nabla^2 n_{e3}) - (\beta + 6 \cdot \sigma) \cdot \nabla^2 n_{e3}] \qquad (4\text{-}24)$$

Substitution of $\nabla^2 n_{e3}$ from Eq 4-23 into Eq 4-24 results in

$$\nabla^2 n_{e4} = (1/4) \cdot [D_e \cdot \nabla^2 (\nabla^2 n_{e3}) - (\beta + 6 \cdot \sigma) \cdot (\beta \cdot n_{e3} + 6 \cdot \sigma \cdot n_{e3} + 4 \cdot n_{e4}) / D_e] \qquad (4\text{-}25)$$

Substituting Eqs 4-18 and 25 into Eq 4-22

$$D_e^2 \cdot \nabla^2(\nabla^2 n_{e3}) - \beta^2 n_{e3} - \beta\cdot(12\cdot\delta\cdot n_{e3} + 8\cdot n_{e4}) - (12\cdot\delta^2 n_{e3} + 4\cdot\omega^2)\cdot n_{e3} - 24\cdot\delta\cdot n_{e4} - 20\cdot n_{e5} = 0 \qquad (4\text{-}26)$$

This procedure is proceeded and the results are summarized below:

$$\begin{aligned}
&n_{e0} = 0 \ ; \\
&n_{e1} = 0 \ ; \\
&n_{e2} = 0 \ ; \\
&n_{e3} = 2\cdot\omega^2\cdot N/3 \ ; \\
&D_e \nabla^2 n_{e3} - (A\cdot\beta + B) = 0 \ ; \qquad (4\text{-}27) \\
&D_e^2 \nabla^2(\nabla^2 n_{e3}) - (A\cdot\beta^2 + 2\cdot B\cdot\beta + C) = 0 \ ; \\
&D_e^3 \cdot \nabla^2(\nabla^2(\nabla^2 n_{e3})) - (A\cdot\beta^3 + 3\cdot B\cdot\beta^2 + 3\cdot C\cdot\beta + D) = 0 \ ; \\
&D_e^4 \cdot \nabla^2(\nabla^2(\nabla^2(\nabla^2 n_{e3}))) - (A\cdot\beta^4 + 4\cdot B\cdot\beta^3 + 6\cdot C\cdot\beta^2 + 4\cdot D\cdot\beta + E) \\
&\qquad\qquad - 120\cdot A\cdot\alpha = 0 \ ; \\
&\qquad\qquad \cdots
\end{aligned}$$

where

$$\begin{aligned}
&A = n_{e3} \ ; \\
&B = (6\cdot\delta)\cdot n_{e3} + 4\cdot n_{e4} \ ; \\
&C = (12\cdot\delta^2 + 4\cdot\omega^2)\cdot n_{e3} + 4\cdot(6\cdot\delta)\cdot n_{e4} + 20\cdot n_{e5} \ ; \\
&D = 8\cdot(-19\cdot\delta^3 + 11\cdot\delta\cdot\omega^2)\cdot n_{e3} + 4\cdot(12\cdot\delta^2 + 4\cdot\omega^2)\cdot n_{e4} \qquad (4\text{-}28) \\
&\qquad + 20\cdot(6\cdot\delta)\cdot n_{e5} + 120\cdot n_{e6} \ ; \\
&E = -960\cdot(\delta^4 + 9\cdot\delta^2\omega^2)\cdot n_{e3} + 4\times 8\cdot(-19\cdot\delta^3 + 11\cdot\delta\cdot\omega^2)\cdot n_{e4} \\
&\qquad + 20\cdot(12\cdot\delta^2 + 4\cdot\omega^2)\cdot n_{e5} + 120\cdot(6\cdot\delta)\cdot n_{e6} + 840\cdot n_{e5} \ ; \\
&\qquad\qquad \cdots
\end{aligned}$$

The results of electron density measurements provide n_{e3}, n_{e4}, ..., when expanded in power series; although it is not possible to perform measurements for t less than 3 μs, the first three equations of Eqs 4-27 act as aguideline for the power series expansion; n_{ei}

can be found by equating n_e to $\sum_{i=3}^{M} n_{ei} \cdot t^i$ at M-2 points.

Having n_{ei}, δ, and ω, the coefficients A, B, C,... can be found from Eq 4-28; it is then possible to solve the system of Eqs 4-27 to find D_e, β, α, and D_p (D_p appears in some equations following those shown in Eqs 4-27).

The difficulty is, however, that the Laplacian of n_{e3} and even its higher order partial derivatives appear in Eqs 4-27 and thus the initial electron distribution, N, should be known. N does, of course, depend on the chamber geometry, the geometry and the position of the uv source, and the pressure.

It is possible to guess reasonable profiles for N and to find the other parameters correspondingly. The fact should also be considered, as was mentioned earlier, that the measured electron densities are averaged in the radial direction of the chamber by the plasma diagnostic device.

To solve Eqs 4-27 for the unknowns let

$$n_{e3} = 2 \cdot \omega^2 \cdot N/3 = f(r,z) \qquad (4\text{-}29)$$

where a cylindrical chamber is considered with z along the axis and r in the radial direction; the origin is assumed to be at the wall end where the uv source is. f is considered to be a function of r and z only because of the azimuthal symmetry. f should be chosen so that it satisfies (and also its Laplacian and its higher order derivatives as appear in Eqs 4-27) the boundary conditions (i.e. they are zero at the chamber walls).

Let

$$K_1 = [(\int_0^{r_0} \nabla^2 n_{e3} \cdot dr) / \int_0^{r_0} n_{e3} \cdot dr]_{z=z_m} ;$$

$$K_2 = [(\int_0^{r_0} \nabla^2(\nabla^2 n_{e3})\cdot dr)/\int_0^{r_0} n_{e3}\cdot dr]_{z=z_m} \; ; \quad (4\text{-}30)$$

$$K_3 = [(\int_0^{r_0} \nabla^2(\nabla^2(\nabla^2 n_{e3})\cdot dr)/\int_0^{r_0} n_{e3}\cdot dr]_{z=z_m} \; ;$$

. . . .

where r_0 is the radius of the chamber and z_m is the distance of the plasma diagnostic device from the uv source. The values are integrated in the r direction since with the mentioned diagnostic methods, only $(\int_0^{r_0} n_e \cdot dr)/r_0$ can be measured.

Substituting from Eqs 4-30 into Eqs 4-27 and manipulating it was found that:

$$\beta = -B/A + K_1 \cdot [(B^2 - A\cdot C)/(K_1^2 - K_2)]^{1/2}/A \; ; \quad (4\text{-}31)$$

$$D_e = (\beta + B/A)/K_1 \; . \quad (4\text{-}32)$$

An equation for α can be similarly obtained. Moreover, some equations can be obtained relating different K_i's to each other, for example

$$K_3 = -2\cdot K_1^3 + 3\cdot K_1\cdot K_2 - [B^2 - A^2\cdot D - 3B\cdot(B^2 - A\cdot C)]\cdot [(K_1^2 - K_2)/(B^2 - A\cdot C)]^{3/2} \quad (4\text{-}33)$$

Eq 4-33 puts a restriction on the functions chosen for the initial electron distribution.

Another parameter helpful in finding the unknowns is the pressure of the gas in the chamber, P; at low enough pressures, as is the case in these experiments, D_e is inversely proportional to P, so let

$$D_e = D_{e0}/P \; ; \quad (4\text{-}34)$$

β is directly proportional to P;

$$\beta = \beta_e \cdot P \quad (4\text{-}35)$$

Substituting from Eqs 4-34 and 35 into Eqs 4-27 it is found that

$$D_{eo} \cdot K_1 = \beta_o \cdot P^2 + (B/A) \cdot P \quad ;$$
$$D_{eo}^2 \cdot K_2 = \beta_o \cdot P^4 + 2 \cdot (B/A) \cdot P^3 + (C/A) \cdot P^2 \; ; \qquad (4\text{-}36)$$
$$\cdots$$

The factors B/A, C/A,... can be found for different pressures, thus it is possible to find how K_1, K_2,... depend on P; considering Eqs 4-30 it is possible to determine accurately the initial electron distribution.

Considering the order of magnitude of D_e, β, and α some simplifying assumptions can be made, as will be illustrated in the following examples.

Experimental Verification

Example 1

As a first example the data obtained by McKen [2] for CO are analyzed. The data are reproduced in Fig 4-1.

The first step is to find n_{ei}; this is simply done by equating n_e to $\sum_{i=3}^{M} n_{ei} \cdot t^i$, or solving the matrix equation

$$\{F\} = [T] \cdot \{W\} \qquad (4\text{-}37)$$

where

$\{F\}$ is a column matrix containing the values of n_e at times $t_1, t_2, \ldots t_{M-2}$.

$[T]$ is a square $(M-2) \times (M-2)$ matrix; its i^{th} row contains the elements $t_i^3, t_i^4, \ldots t_i^{M-2}$.

$\{W\}$ is a column matrix containing $n_{e3}, n_{e4}, \ldots n_{eM-2}$.

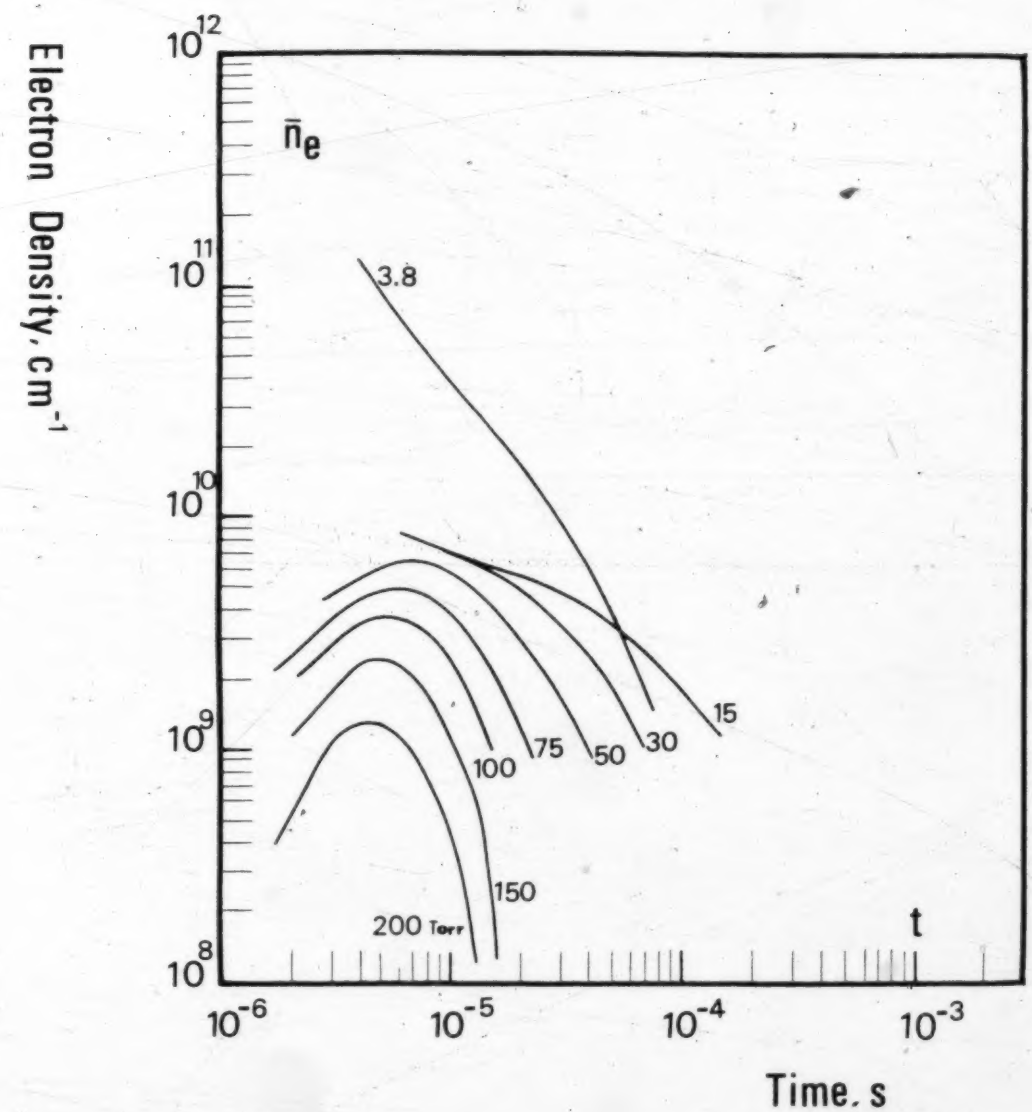

Fig 4-1 Photo-electron density vs. time in CO.

cylindrical chamber : r_c = 15 cm ; L = 28.5 cm ; Z_m = 10 cm

To find A, B,..., E of Eqs 4-28 it is convenient to define

$$\{Y\} = \begin{Bmatrix} 1 \\ 4 \\ 20 \\ 120 \\ 840 \end{Bmatrix} \tag{4-38}$$

and

$$\{V\} = \begin{Bmatrix} -960\cdot(\sigma^4+9\cdot\sigma^2\cdot\omega^2) \\ 8\cdot(-19\cdot\sigma^3+11\cdot\sigma\cdot\omega) \\ (12\cdot\sigma^2+4\cdot\omega^2) \\ 6\cdot\sigma \\ 1 \end{Bmatrix} \tag{4-39}$$

Considering the above definitions the following APL program is written to find A, B,..., E; the dyadic function CF takes F and t_i as its arguments and calculates the desired quantities. In the program t_i is represented by TI, a vector with the elements t_1, t_2,...

```
∇TI  CF  F
[1] T←TI∘.*2+⍳M-2
[2] W←F⌸T
[3] W←W×Y
[4] A←1↑W
[5] B←(2↑W)+.×3↓V
[6] C←(3↑W)+.×2↓V
[7] D←(4↑W)+.×1↓V
[8] E←W+.×V ∇
```

The results are shown in Table 4-1.

Comparing the values of B/A to the order of magnitude of β, $10^{-3}\ \mu s^{-1}$, β can be neglected and Eq 4-32 reduces to

$$D_{e0} \cdot K_1 \approx (B/A) \cdot P. \qquad (4\text{-}40)$$

Similarly, the other equations in Eq 4-27 can be simplified. In other words, α and β are so small that the whole process is initially diffusion controlled.

Fig 4-2 shows a plot of $(B/A) \cdot P$ vs. P. It can be seen that a parabolic function fits the points. There is a spread in the data points; the main cause of this spread is that the voltage applied to the spark plug is not quite constant, causing a spread in the ionization level. In later experiments (example three below) an attempt was made to stabilize the voltage applied to the spark plug as much as possible, and much more satisfactory results were obtained.

To find K_1, many reasonable initial electron density profiles were assumed. The results of computer calculations indicated that, for the use of Eq 4-1, the initial electron density can be assumed constant in the radial direction of the chamber; so

$$K_1 = [(d^2 \bar{n}_{e3} / dz^2) / \bar{n}_{e3}]_{z=z_m} \qquad (4\text{-}41)$$

In order for K_1 to be of second order in P, n_{e3} should be of the form

$$\bar{n}_{e3} = f(z) \cdot e^{-\eta \cdot P \cdot z} \qquad (4\text{-}42)$$

It is amazing to notice that this is similar to the distribution obtained by Babcock et al. [3] by completely different procedures.

P, Torr	50	75	100	150	200
A	1.23×10^{9}	3.27×10^{9}	2.65×10^{9}	1.29×10^{9}	9.81×10^{8}
B	4.30×10^{9}	-6.77×10^{9}	-6.26×10^{9}	-4.83×10^{9}	3.05×10^{8}
C	1.13×10^{11}	3.45×10^{11}	2.82×10^{11}	2.04×10^{11}	1.00×10^{10}
D	1.34×10^{12}	1.65×10^{12}	1.26×10^{12}	8.79×10^{11}	1.01×10^{11}
E	-6.16×10^{12}	-2.47×10^{13}	-2.04×10^{13}	-1.49×10^{13}	-4.12×10^{11}
(B/A)·P	174.0	-155.1	-236.5	-378.0	623.0
ln(A)	20.93	21.91	21.70	20.98	20.70

Table 4-1 The results of computer calculations for the data of Fig 4-1.

time : μs,

length : cm

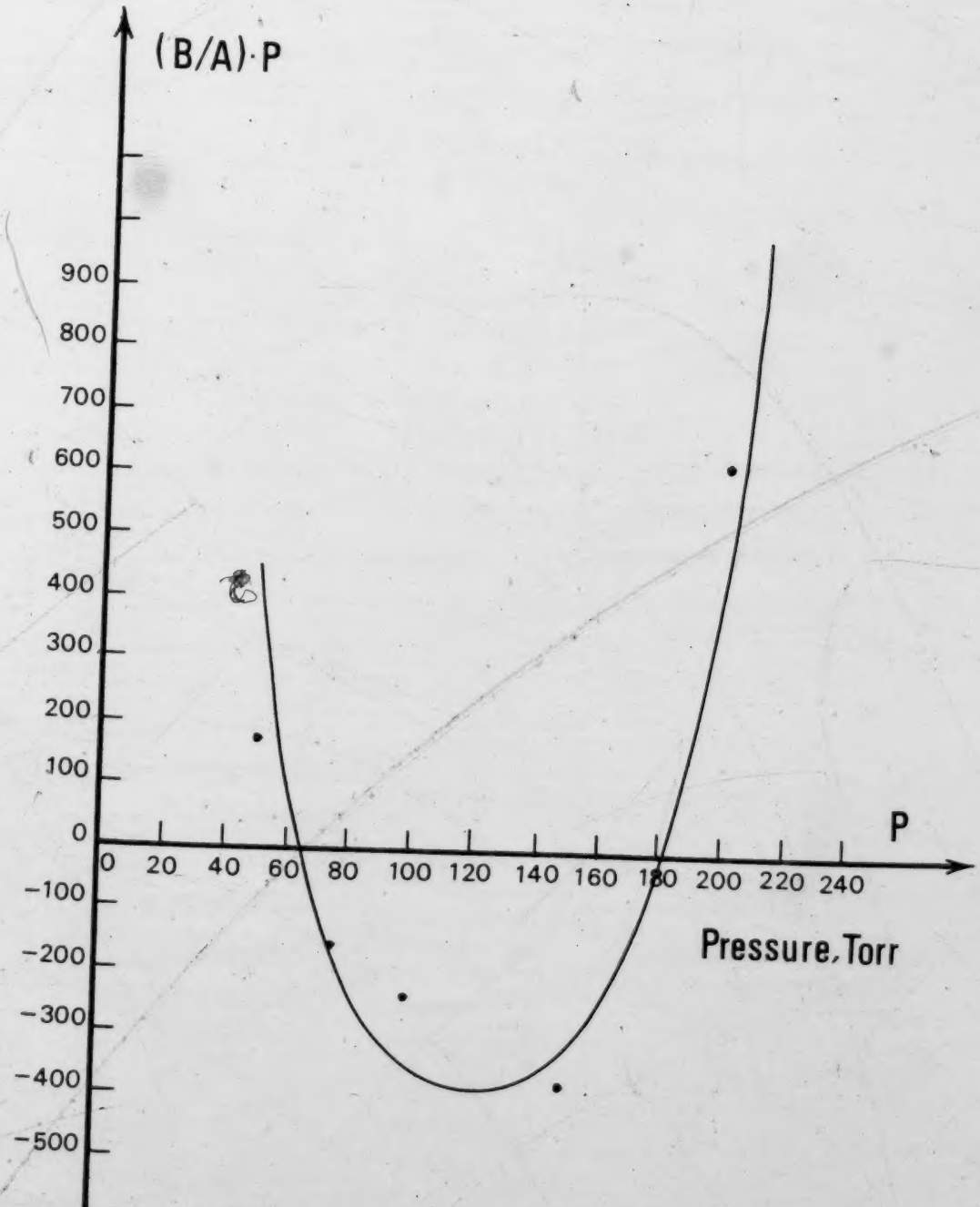

Fig 4-2 Variation of (B/A)·P with pressure.
(for the data of Fig 4-1)

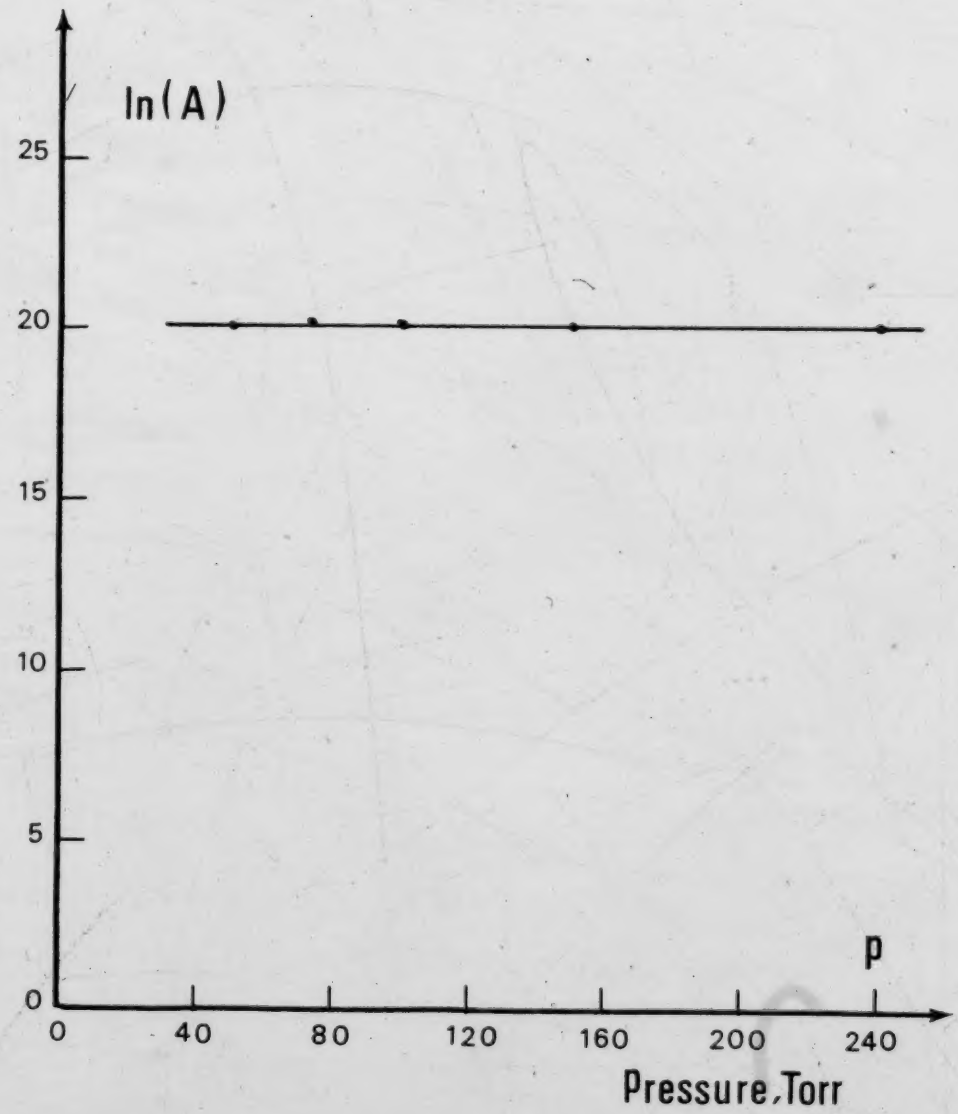

Fig 4-3 ln(A) vs. pressure.
for the data of Fig 4-1

From Eqs 4-41 and 42

$$K_1 = (\eta \cdot P)^2 - 2 \cdot [f'(z_m)/f(z_m)] \cdot (\eta \cdot P) + [f''(z_m)/f(z_m)] . \quad (4\text{-}43)$$

The terms in the square brackets in Eq 4-43 are geometrical factors depending on the chamber geometry and the position of the uv source. From Eq 4-40 and the data of Fig 4-2, it is possible to find these geometrical factors and η, knowing D_{eo} for CO. Once the geometrical factors are found, the chamber is calibrated and η and D_{eo} can be found for any other gas, provided z_m is kept fixed.

Following this procedure, η was found to be 0.2585 cm^{-1}. $Torr^{-1}$ for CO; $(\eta \cdot P)^{-1}$ is a measure of the penetration depth of the uv radiation in the gas at pressure P.

The geometrical factors are

$$f'(z_m)/f(z_m) = 30.7 \quad cm^{-1} , \quad (4\text{-}44)$$

$$f''(z_m)/f(z_m) = 745 \quad cm^{-2} . \quad (4\text{-}45)$$

Another important result can be deduced from Table 4-1. A is the initial electron density at z_m multiplied by a constant (Eqs 4-27 and 28). It is interesting to see how A changes with pressure.

It is noted that in McKen's [2] data the uv source is located in the chamber without a window separating the two. Thus as the pressure increases the intensity of the uv source increases (Refs [1] and [2]), but at the same time the penetration depth decreases (Eq 4-42). Fig 4-3 shows a plot of ln(A) vs. P; this is a straight line indicating that the intensity of the uv source resulting in photoionization increases exponentially with the pressure in the pressure range in which the experiments are performed.

$$A = g(z_m) \cdot e^{\gamma \cdot P} \cdot e^{-\eta \cdot P \cdot z_m} \qquad (4\text{-}46)$$

From the slope of ln(A) vs. P, can be found to be

$$\gamma = 2.625 \quad \text{Torr}^{-1}$$

γ depends both on the intensity of the uv source and the ionization level of the gas used.

Example 2

In the second example, another data set obtained by McKen [2] is analyzed. The data are reproduced in Fig 4-4.

Fig 4-5 shows a plot of (B/A)·P vs. P; from Fig 4-5 and the procedure explained in Example 1

$$D_{eo} = 0.0388 \quad \text{Torr} \cdot \text{cm}^2 \cdot \mu\text{s}^{-1}$$

$$\eta = 1.23 \quad \text{cm}^{-1} \cdot \text{Torr}^{-1}$$

In Fig 4-6 ln(A) vs. P is plotted; it is found that

$$\gamma = 12.384 \quad \text{Torr}^{-1}$$

Example 3

The data of example three (Fig 4-7) are obtained by the experimental setup explained in Chapter Two. The plasma diagnostic device is the microwave interferometer (Fig 2-8).

In Figs 4-8 and 9 (B/A)·P and ln(A) are plotted vs. P. The diffusion coefficient for N_2 is available so that the chamber can be calibrated; the following results are obtained.

$$f'(z_m)/f(z_m) = 4.45 \quad \text{cm}^{-1}$$

$$f''(z_m)/f(z_m) = 84.7 \quad \text{cm}^{-2}$$

$$\eta = 0.594 \quad \text{cm}^{-1} \cdot \text{Torr}^{-1}$$

$$\gamma = 2.99 \quad \text{Torr}^{-1}$$

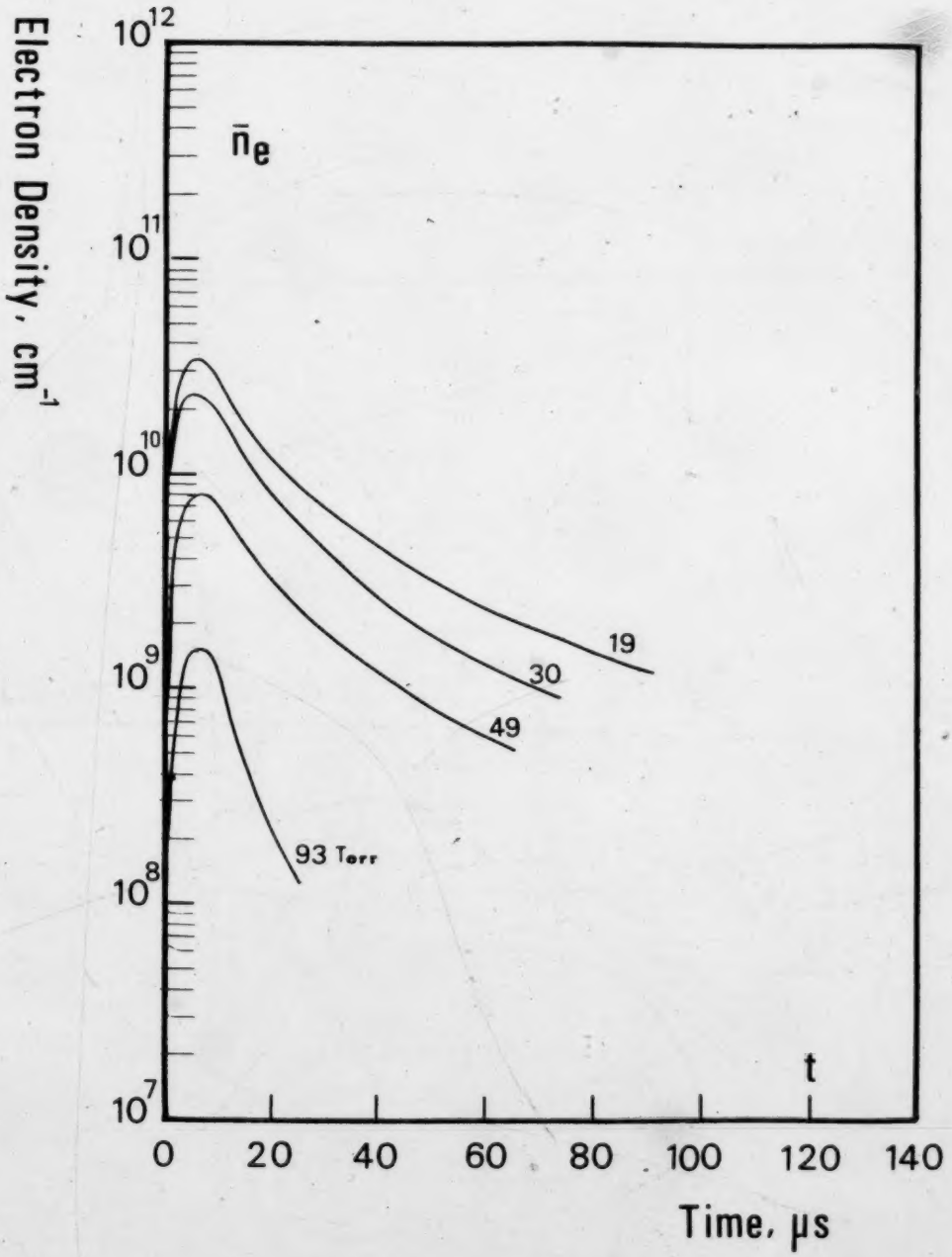

Fig 4-4 Photo-electron density vs. time in Tri-n-propyl Amine.

CO_2: N_2: He = 1:1:3 passed through bubble chamber containing Tri-N-Propyl Amine chamber geometry: same as Fig 4-1

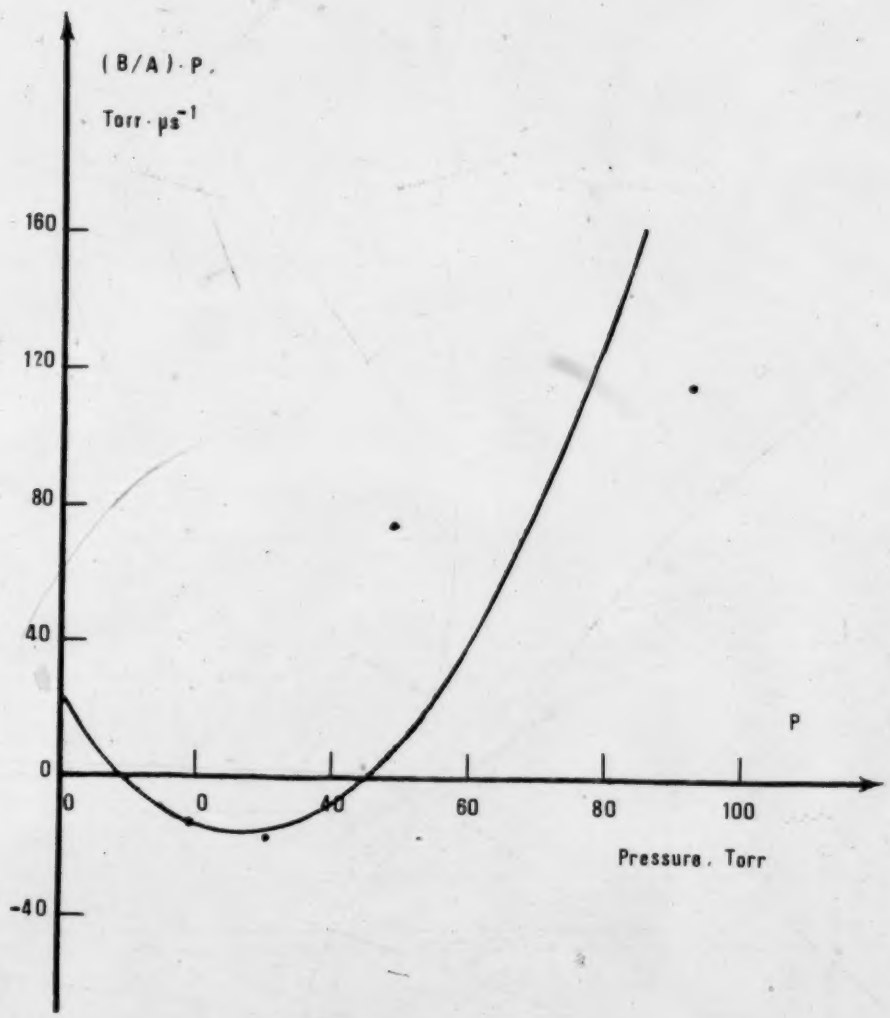

Fig 4-5 (B/A)·P vs. pressure.
for the data of Fig 4-4

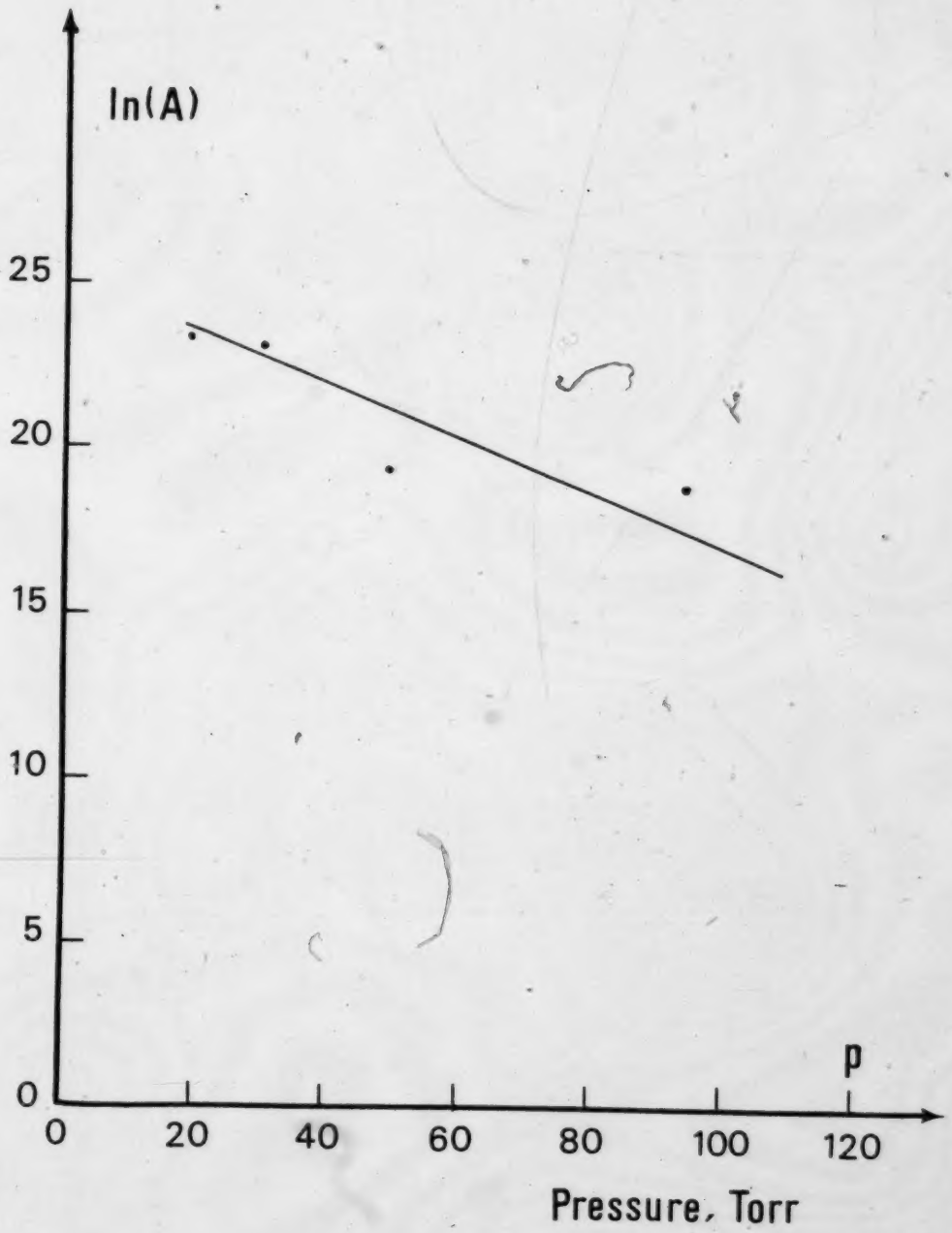

Fig 4-6 ln(A) vs. pressure for the data of Fig 4-4.

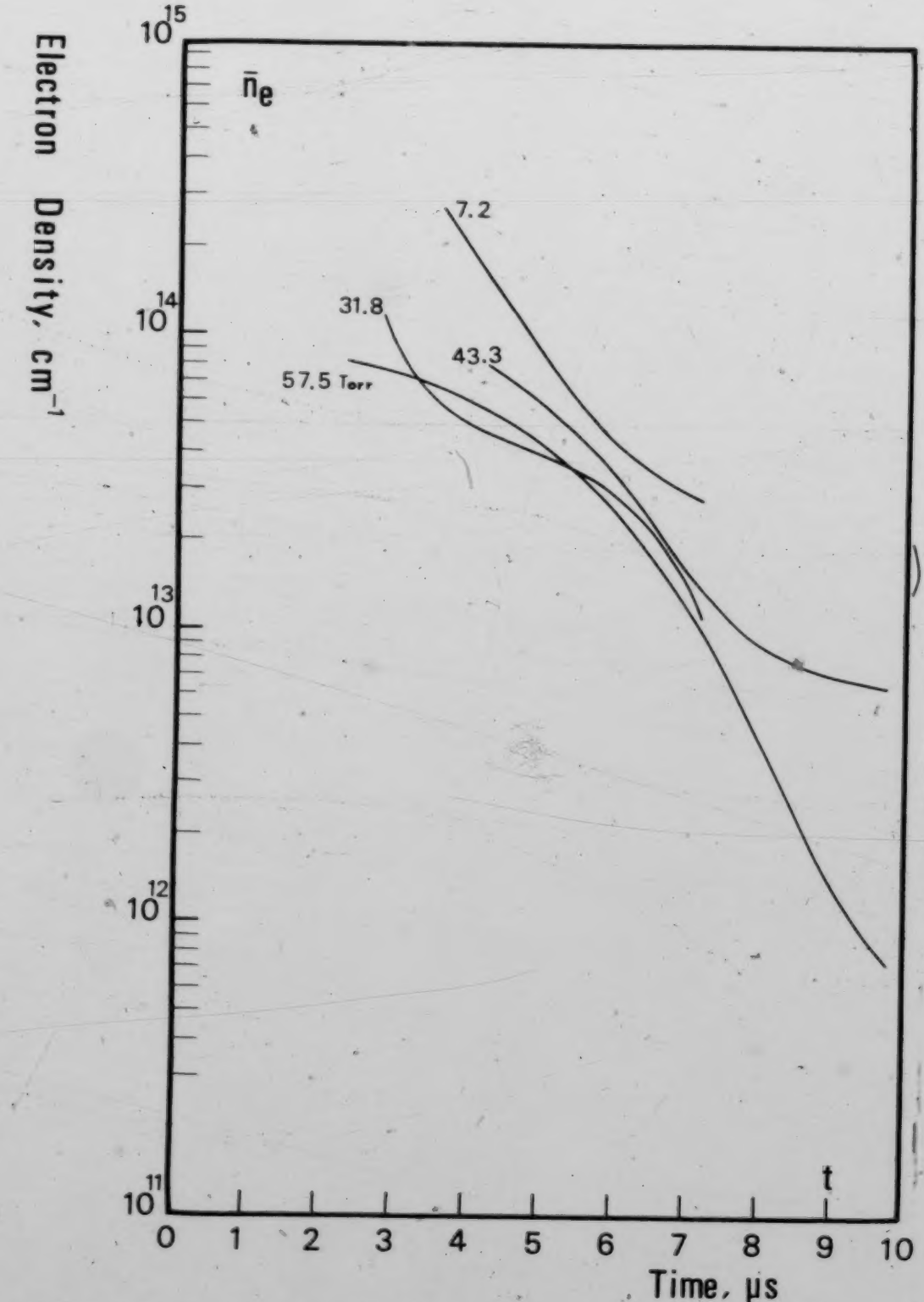

Fig4-7 Photo-electron density vs. time in N_2.
experimental conditions: same as in Fig3-3

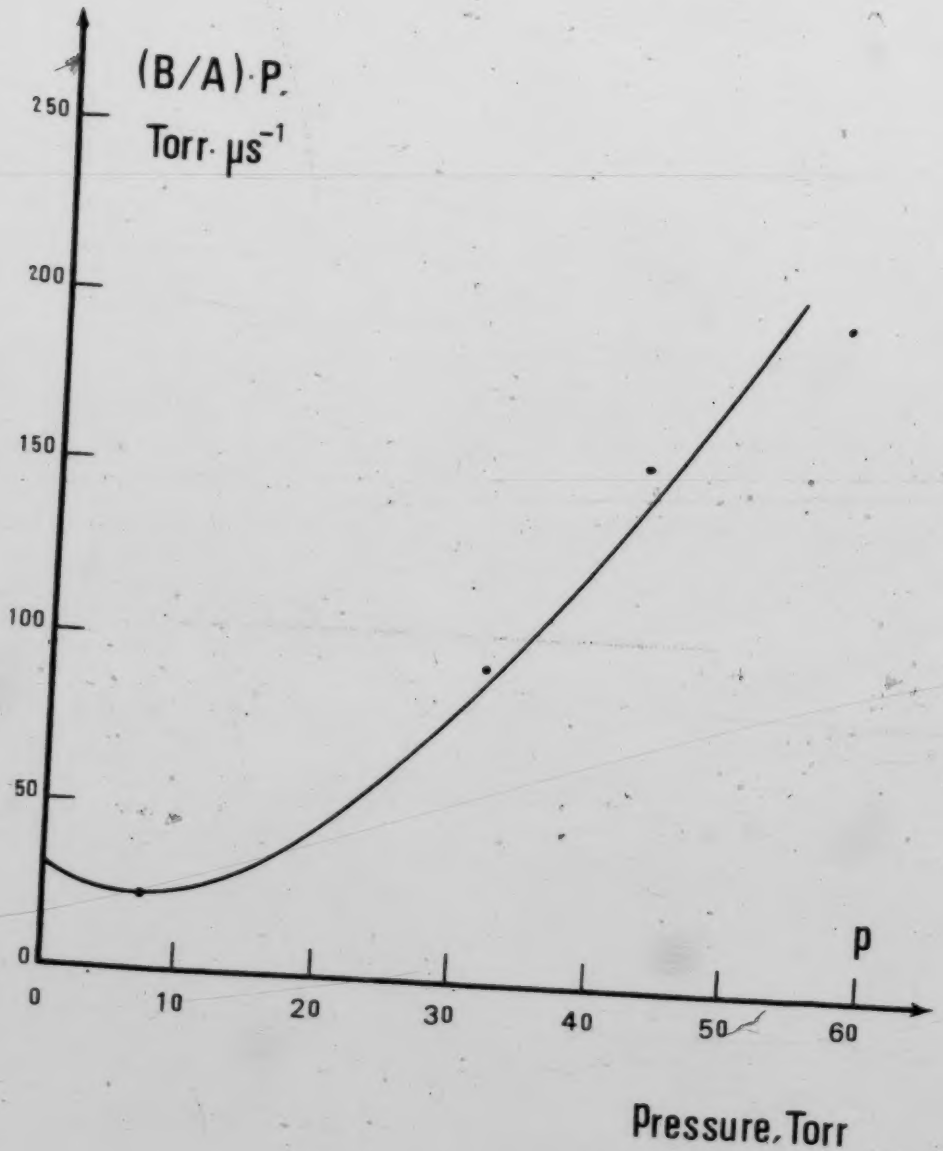

Fig 4-8 (B/A)·P vs. pressure.
for the data of Fig 4-7

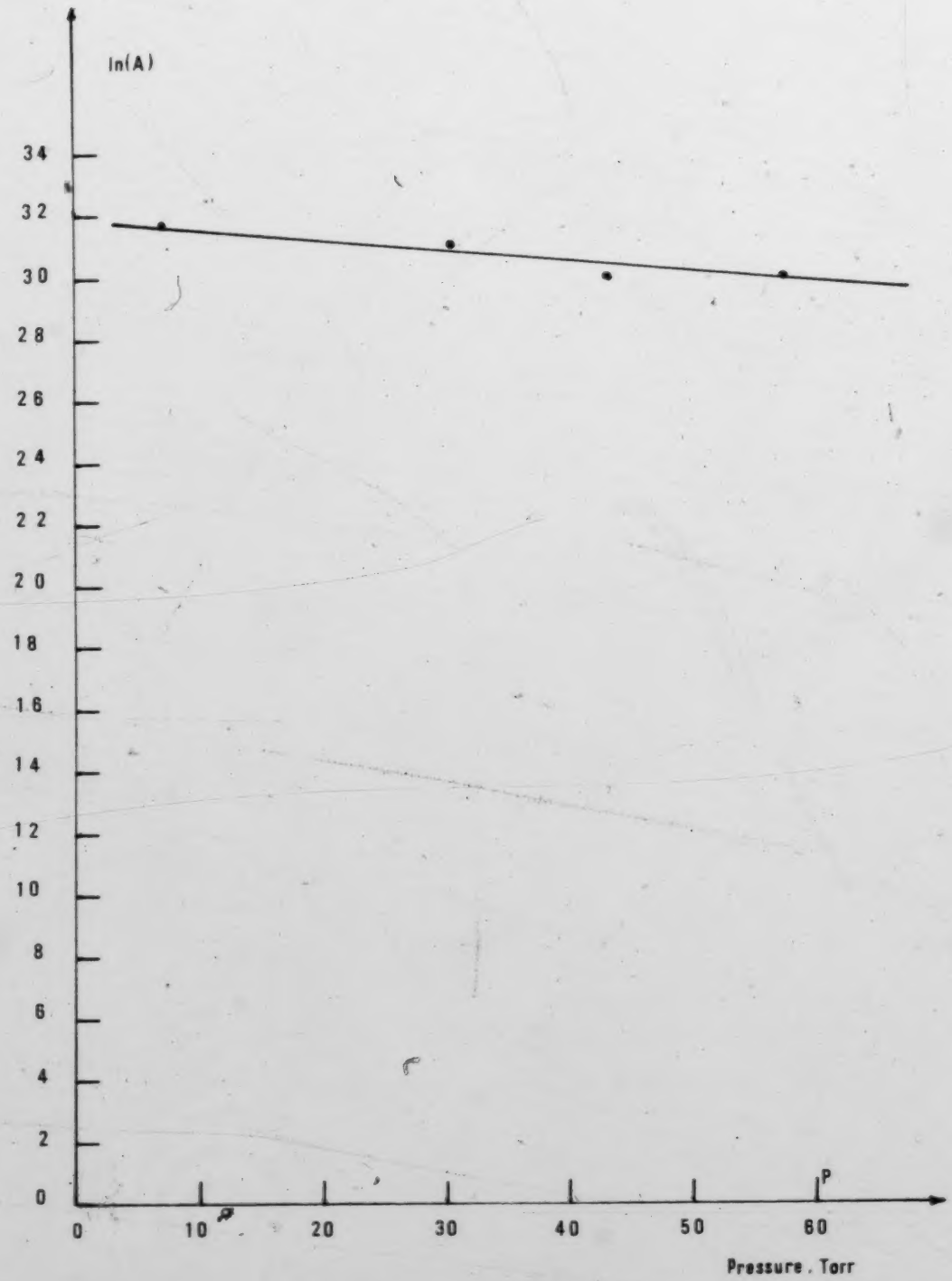

Fig 4-9 ln A vs. pressure for the data of Fig 4-7.

Conclusions

In the above examples it is noticed that the electron diffusion plays an important role in the uv-preionized lasers. In contrast to the conclusions reached by others, it seems that the delay between the uv source and the main discharge is mainly due to the fact that a delay is needed for the photo-electrons to be distributed evenly between the discharge electrodes; the delay, of course, depends on the laser geometry and the location of the uv source.

The theoretical method, however, is quite general and can handle even those complicated cases in which attachment and recombination also play an important role.

The most difficult task in the numerical technique, is the determination of the initial electron density distribution, together with its Laplacian and higher order partial derivatives appearing in Eq 4-30. To simplify this task and to improve the accuracy of the results, the geometry of the chamber can be changed: the chamber can be a rectangular parallelepiped, since, in that geometry, the Laplacian and the other derivatives will acquire simpler forms. In additions, many spark plugs all ignited simultaneously, can be evenly located in one face of the chamber - as in actual laser designs - to make the electron density vary only in one direction. This simplifies the differentiations of Eqs 4-30 even more. Moreover, if the plasma diagnostic device is aligned in the direction in which the electron density is uniform, then the electron density measurements become more accurate; the electron density, and

not its average in a direction, is measured and the integrations in Eqs 4-30 can be omitted.

In this way, the average electron density will also be increased, making the use of laser diagnostic techniques possible; laser diagnostic techniques are much more suitable for these measurements, due to their small wavelength compared to the microwaves; the laser light can be focused on much smaller cross-sectional areas, resulting in much more accurate electron density measurements.

Finally, the r.f. noise generated by the uv source will not affect the laser output, making the measurements possible soon after the ignition of the uv source.

REFERENCES

[1] D.C. McKen, H.J.J. Seguin, and J. Tulip, IEEE J. Quantum Electron, Vol. QE-12, No. 8, PP. 470-482, Aug. 1976.

[2] D.C. McKen, Ph.D. Thesis, Dep. of Electrical Eng., U of A, Spring 1976.

[3] R.V. Babcock, I.L. Liberman, and W.D. Partlow, IEEE J. Quantum Electron, Vol. QE-12, No. 1, Jan. 1976.

[4] R. Burnham, and N. Djeu, Appl. Phys. Lett., Vol. 29, No. 11, PP. 707-709, Dec. 1976.

[5] D.E. Rothe and R.A. Gibson, Optics Com., Vol. 22, No. 3, PP. 265-268, Sep. 1977.

[6] J. Hsia, Appl. Phys. Lett., Vol. 30, No. 2, PP. 101-103, Jan. 1977.

[7] J.E. Velazco and D.W. Setser, J. Chem. Phys., Vol. 62, No. 5, PP. 1990-1991, Mar. 1975.

[8] C.A. Brau and J.J. Ewing, J. Chem. Phys., Vol. 63, PP. 4640, 1976.

[9] M.L. Bhaumik, R.S. Bradford, and E.R. Ault, Appl. Phys. Lett., Vol. 28, No. 1, PP. 23-24, Jan. 1976.

[10] T.H. Dunning and P.J. Hay, Appl. Phys. Lett., Vol. 28, No. 11, PP. 649-51, June 1976.

[11] Matheson Gas Products, General Chemical Data Sheet TA-85411.

[12] S. Shammas and H.J.J. Seguin, (to be published).

[13] H.J.J. Seguin, J. Tulip, and D.C. McKen, IEEE J. Quantum Electron, Vol. QE-10, PP. 311-319, Mar. 1974.

[14] W. Lochte-Holtgreven, "Plasma Diagnostics", PP. 478-549, John Wiley & Sons, Inc., New York, 1968.